

# Informative Multiview Planning for Underwater Sensors

Jaejeong Shin , *Member, IEEE*, Shi Chang , *Student Member, IEEE*, Joshua Weaver, *Member, IEEE*, Jason C. Isaacs, *Member, IEEE*, Bo Fu , *Member, IEEE*, and Silvia Ferrari , *Senior Member, IEEE*

**Abstract**—Many modern imaging sensors must obtain multiple looks or “views” of a target at different orientations to automatically classify it with high confidence. Therefore, when tasked with classifying many targets, a mobile sensor may need to travel a long distance to change its position and orientation relative to every target, resulting in costly and time-consuming operations. This article presents a novel and general approach, referred to as informative multiview planning (IMVP) that simultaneously determines the most informative sequence of views and the shortest path between them. The approach is demonstrated on an underwater multitarget classification problem in which a sidescan sonar installed on an unmanned underwater vehicle must classify all targets in minimum time. Simulation and experimental results show that IMVP can achieve the same, or better, classification performance in half the time of existing multiview path planning methods. Also, by determining the most informative views and the shortest path between them, IMVP significantly improves classification efficiency, classification confidence level, as well as performance robustness.

**Index Terms**—Autonomous sensors, classification, confidence level (CL), information gain, information-driven path planning, minimum-time search, sonar, traveling-salesman problem (TSP), underwater imaging, unmanned vehicles, viewpoint planning.

## I. INTRODUCTION

**M**ANY modern imaging sensors, such as underwater sonar or cameras, require multiple looks or “views” of the target before they are able to classify it with a high level of confidence. By changing the sensor position and orientation relative to each target, different information about target features, such as shape and size, may be obtained and fused to better infer the target class. Mobile platforms, such as unmanned vehicles, are often utilized to allow the sensor to travel around an object and record multiple images from different viewpoints. When a sensor must classify multiple targets distributed over a large region obtaining multiple views may require traveling over a

long distance to visit multiple positions and orientations relative to each target, resulting in costly and time-consuming operations that may potentially exceed the battery life of the vehicle.

Multiple aspect coverage (MAC) and adaptive MAC algorithms have been developed to solve multiview path planning problems by first generating a star-like path around every target and, then, computing the shortest route between them [1], [2]. MAC-type algorithms rely on the user choosing the number of views required for every target, and, subsequently, picking a subset of vehicle-heading angles by sampling uniformly the 180° range of all possible angles. Another solution approach proposed in [3] connects multiple viewing angles decided *a priori* by means of Dubins curves that are reachable based on the vehicle kinematic constraints. The sensor’s next viewing angle is chosen based on experimental results and, then, the path is planned such that every target is visited again with the same viewing angle. All of these existing algorithms seek to reduce the task-completion time by finding the shortest path between multiple views decided *a priori*. Because they do not take into account individual target characteristics, they may obtain too-many or too-few images resulting in paths that are too time consuming or have low classification accuracy (CA), respectively. Moreover, because they rely on user intervention, they may be difficult to automate or adapt to heterogeneous classification and environmental conditions.

Along a different line of research, next-best-view approaches have been developed to determine what is the next most informative view for a target, based on information gain [4], [5], or partially observable Markov decision processes [6]. Information-driven path-planning approaches, reviewed comprehensively in [7], take into account both the sensing objective and the vehicle kinodynamic constraints to simultaneously optimize the sensor performance and the energy consumption. Finding the most efficient sensor path is especially critical in underwater applications because, due to limited communications and rapidly changing sea conditions, the vehicles must travel back to the host ship to update their information state and complete each operation as quickly as possible. Although existing information-driven path-planning methods have been shown highly effective at optimizing the performance of mobile sensors [7]–[12], these existing methods are not directly applicable to multiview planning because they assume the information gain is independent of target-relative position and orientation. Many imaging sensors, such as cameras, active sonar, and radar, interpret a return signal (e.g., acoustic or optical wave) that

Manuscript received September 9, 2020; revised June 14, 2021; accepted October 1, 2021. Date of publication May 24, 2022; date of current version July 13, 2022. This work was supported by Office of Naval Research under Grant N00014-15-1-2595 and Grant N00014-19-1-2144. (*Corresponding Author: Silvia Ferrari.*)

**Associate Editor: F. Zhang.**

Jaejeong Shin, Shi Chang, Bo Fu, and Silvia Ferrari are with the Sibley School of Mechanical and Aerospace Engineering, Cornell University, Ithaca, NY 14850 USA (e-mail: js3456@cornell.edu; sc2892@cornell.edu; bofu11010219@gmail.com; ferrari@cornell.edu).

Joshua Weaver and Jason C. Isaacs are with the Naval Surface Warfare Center, Panama City, FL 32407 USA (e-mail: joshua.n.weaver@navy.mil; jason.c.isaacs1@navy.mil).

Digital Object Identifier 10.1109/JOE.2021.3119150

bounces off an object of interest and, thus, the quality of their measurements heavily depends on their aspect angle. Furthermore, the image quality and the ability to recognize the object also depend on the object's shadow and self-occlusions, which vary with both sensor position and orientation.

This article develops a novel and general approach for informative multiview planning (IMVP) that simultaneously determines the best sensor views for each individual target, based on prior information, and plans the optimal path between them. The IMVP approach developed in this article takes into account the sensor's field-of-view (FOV) and Bayesian measurement model, as well as the target's position and orientation, to construct novel C-target regions and information gain functions applicable to imaging sensors. It is shown that, for a continuous and bounded sensor FOV, the optimal path can be found by solving a generalized traveling-salesman problem (TSP) [13], [14]. Due to its high complexity, many approximate and ad-hoc solutions have been proposed for generalized TSPs (GTSPs) [15]–[18]. One of the most common simplifications is to assume that the regions of interest are pairwise disjoint [19]–[21]. However, in informative multiview path planning, intersecting regions are often the most valuable because they allow the sensor to obtain images from multiple targets in a single pass.

The IMVP approach builds on several novel contributions that allow us to first formulate and, then, solve the GTSP based on all available sensor and target information. Novel contributions in computational geometry (Section IV) allow for the efficient construction of helicoidal C-targets and transcription of the path planning problem into a new generalized TSP with intersecting neighborhoods. A new approximate solution algorithm is developed (Section V) to exploit the neighborhood intersections, thus prioritizing multitarget imaging while reducing computational complexity (Section VII-C). This novel IMVP approach is demonstrated on a mobile sidescan imaging sonar application in which the sensor must classify multiple underwater objects previously detected by an initial survey.

Imaging sonar is a powerful tool that is utilized in a variety of underwater tasks ranging from commercial applications, such as ship hull inspection, to environmental research, such as bathymetric mapping, biomass estimation, and demining [22]–[26]. As a result, many sonar processing algorithms, including convolutional neural networks (CNNs), have been developed and demonstrated for automatic target detection (ATR) and classification, by learning correlations between characteristic highlight-shadow patterns and physical object features such as shape, size, and orientation [27]–[31]. Because sonar images are highly dependent on environmental conditions and sensor-target aspect angle [32], high-quality classification requires fusing multiple images obtained by different viewpoints [33]–[35]. Hence, the effectiveness of the IMVP approach is demonstrated both experimentally and numerically by using a high-fidelity physics-based mobile sidescan sonar closed-loop simulation developed by coauthor Isaacs. The mobile sidescan sonar is simulated by generating images obtained from the sonar FOV, integrated with a dynamic model of a REMUS 100 vehicle, and by  $\omega - k$  beamforming of the time-domain signals [28], [29],

[36], [37]. The results in Section VII show that the IMVP approach significantly outperforms existing methods by achieving the desired classification performance in some cases in half the travel time. In addition to improving classification efficiency and confidence gain by up to 88% and 91%, respectively, IMVP also provides much higher performance robustness than existing algorithms for different classification databases, target layouts, and environmental conditions. By determining the number of views and aspect angles based on their information value and, simultaneously, considering the problem geometry, the sensor paths obtained by IMVP are not only shorter but also produce sonar images that contain on average many more contacts and provide higher quality ATR. Finally, autonomous vehicle architecture (AVA) simulations and sea tests were conducted by coauthor Weaver on the NSWC unmanned underwater vehicle (UUV) swimming in the Saint Andrew Bay area near Panama City, FL, USA (see Sections VII-A–VII-D). The sea tests showed that the real REMUS 100 not only was able to execute the IMVP optimal path, but also outperformed the AVA simulation results under all performance metrics.

## II. PROBLEM FORMULATION

This article considers the problem of planning a path for an underwater imaging sensor deployed onboard a UUV for the purpose of classifying multiple underwater objects in minimum time. This problem is relevant to many underwater sensing applications involving mobile directional sonar and many stationary targets distributed in a large region of interest (ROI). Because acoustic measurements are greatly influenced by the relative sensor position and orientation, most underwater targets require many views before they can be accurately classified, resulting in time-consuming and costly operations. Before a directional sonar, such as a forward-looking or sidescan sonar, is implemented, the ROI is typically surveyed using long-range sensors that provide a rudimentary estimate of target position and orientation. Subsequently, a directional sensor installed on a UUV is implemented to obtain multiple images or “looks” of every object, until a desired confidence level (CL) is achieved by the target classification algorithm [1], [38]. As a result, the time and power required to properly classify multiple targets are highly dependent on the UUV path. Furthermore, modern sensors may be equipped with real-time ATR capabilities. In this case, the UUV path may be updated online based on the local environmental conditions, such that the total number of images and their viewpoints are planned optimally for every object.

This article presents a new underwater sensor planning approach to compute minimum-time paths for classifying multiple underwater targets within a desired CL. The methods presented are potentially also applicable to online adaptive path planning and to other directional sensors, such as cameras or synthetic aperture radar. The approach is presented for an underwater sonar installed on a UUV that must travel in a 3-D ROI,  $\mathcal{W} \subset \mathbb{R}^3$ . For illustration purposes, in this article it is assumed that  $n$  underwater targets are distributed on a flat seabed, such that the effects of sloped and uneven bathymetry, e.g., layover, may

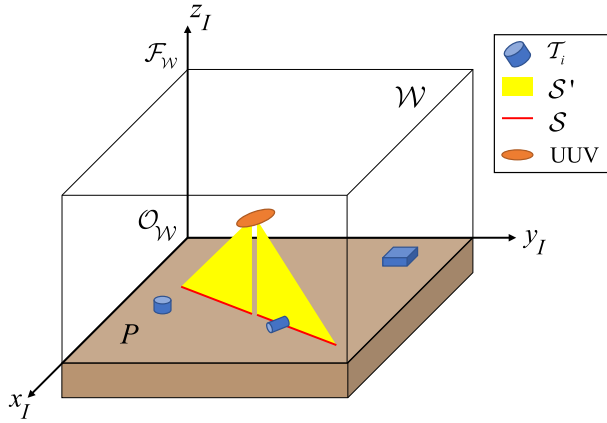


Fig. 1. ROI and key geometrical constructs.

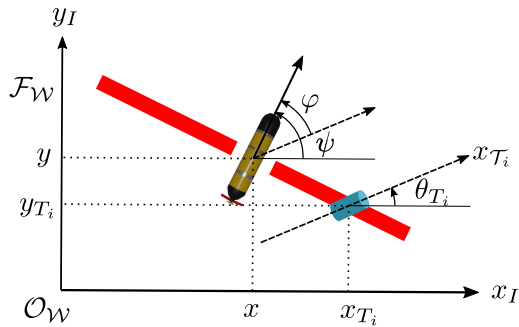


Fig. 2. Definition of target orientation and aspect angle for a UUV-based sonar.

be neglected. Let an inertial frame  $\mathcal{F}_W$  with origin  $\mathcal{O}_W$  be embedded in  $\mathcal{W}$  such that the  $x_I y_I$ -plane contains the seabed of interest denoted by a plane  $P \subset \mathbb{R}^3$  (see Fig. 1).

Every target in  $P$  is characterized by unknown geometries  $\mathcal{T}_1, \dots, \mathcal{T}_n$ , where  $\mathcal{T}_i \subset \mathcal{W}$  is a compact set for  $i = 1, \dots, n$ , and its inertial position, estimated during presurveying, is denoted by  $\mathbf{x}_{T_i} = [x_{T_i} \ y_{T_i}]^T$ . Letting  $\mathcal{F}_{T_i}$  denote a local reference frame embedded in  $\mathcal{T}_i$ , the target *orientation*,  $\theta_{T_i}$ , can be defined as the angle between  $x_{T_i}$ -axis and  $x_I$ -axis (see Fig. 2). Due to the nature of acoustic measurements, the image constructed by the sensor is highly dependent on the so-called *aspect angle*, defined as the off-normal angle between the target and the sensor orientations, measured relative to the sonar centerline and denoted by  $\varphi$  (see Fig. 2). Therefore, the target state is given by  $\mathbf{q}_{T_i} = [x_{T_i}^T \ \theta_{T_i}]^T$ , for  $i = 1, \dots, n$ , and must be estimated to optimize the quality of the sonar imagery.

Consider the benchmark problem in which the UUV-based sonar is used to classify all  $n$  targets and, possibly, estimate the  $f$  target features, such as target geometry, size, and texture. Every target feature can be represented by a categorical random variable  $X_{ij} \in \mathcal{X}_j$ , where  $\mathcal{X}_j$  is the discrete and finite range of the  $j$ th feature ( $j = 1, \dots, f$ ). Then, the feature set of the  $i$ th target is denoted by  $X_i = \{X_{i1}, \dots, X_{if}\}$ . The target classification is denoted by another categorical variable,  $Y_i \in \mathcal{Y}$ , with discrete and finite range  $\mathcal{Y} = \{y_1, \dots, y_c\}$ . Both target features and classification variables are viewed as discrete random variables. But

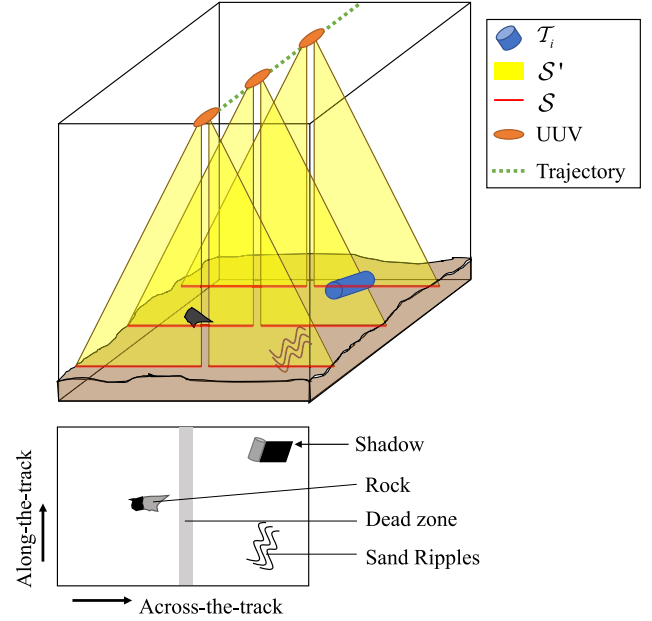


Fig. 3. Sidescan sonar image construction and sensor FOV.

while the features may be estimated from the target sonar image, the classification variable is hidden and must be inferred from the target features (Section III). Therefore, the ATR algorithm must carry out feature estimation and target classification for every new sonar image obtained by the UUV. By optimizing the sonar viewing angle and by taking into account the geometry of the FOV, the approach presented in this article not only minimizes classification time but also minimizes the number of images required, thus minimizing computing and power requirements.

For illustration purposes, the approach developed in this article is presented for a sidescan sonar. However, the approach can be easily extended to other underwater imaging sensors such as sector-scan sonar and synthetic-aperture sonar [39]. Consider the case in which a pair of sidescan sonar sensors is installed on each port and starboard side of the UUV. The sensor FOV is defined as the region in which target measurements can be obtained [7], [40]. Each sensor transmits a narrow fan-shape acoustic pulse, whose geometry is denoted by  $S' \subset \mathcal{W}$ . As the UUV moves forward,  $S'$  sweeps the seabed and a sonar image matrix is constructed by stacking the interpreted data from successive scan lines on the seabed (see Fig. 3). Because all the targets live in  $P$ , the sonar FOV can be reduced to the two-dimensional region  $\mathcal{S} = S' \cap P$ , as shown in Fig. 3. By considering the FOV position and geometry relative to the UUV and the targets, the sensor path and viewpoints can be optimized based on prior target information and ATR measurement process.

As shown in [7], [10], [11], [40]–[44], the sonar ATR and measurement process can be modeled by a probabilistic sensor model in the form of a joint probability mass function (PMF) learned from data (Section III). Without loss of generality, let the set  $Z_i(k)$  denote the sensor measurements obtained from target  $i$  at time instant  $t_k$ . The sensor mode and relevant

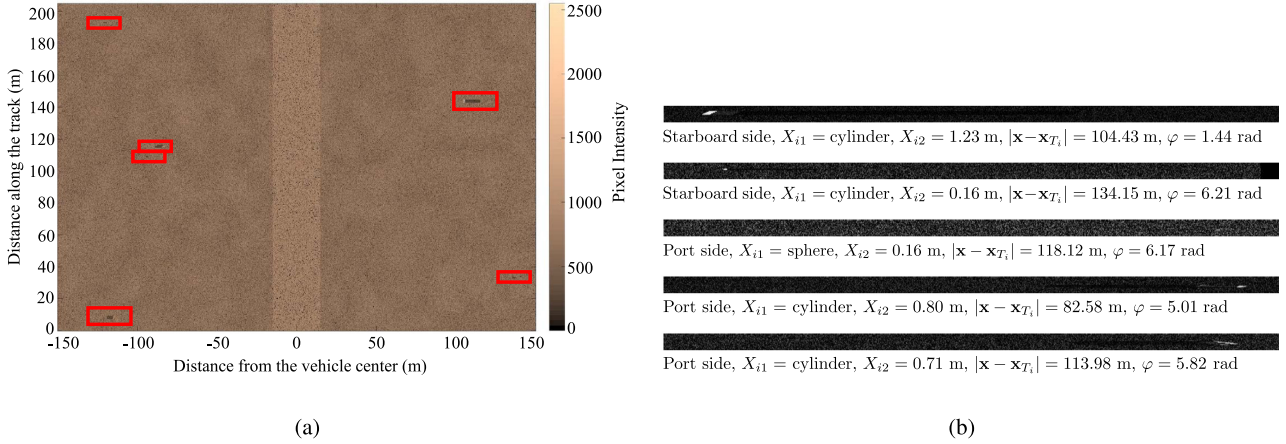


Fig. 4. (a) Example of raw sonar image matrix, where each red box indicates a detected object. (b) Examples of sonar image segmentations and corresponding features extracted via CNN-SVM (adapted from [42], with permission).

environmental conditions at  $t_k$  are denoted by  $\Lambda_i(k)$ . In this article,  $\Lambda_i(k)$  consists of the sonar viewing angle and relative target position, both of which can be estimated by an onboard localization algorithm. Then, with the evidence at  $t_k$  denoted by  $E_i(k) = \{Z_i(k), \Lambda_i(k)\}$ , the learned PMF model can be factorized as follows:

$$p(Z_i, X_i, Y_i, \Lambda_i) = p(Z_i | \Lambda_i, X_i) p(X_i | Y_i) p(Y_i) p(\Lambda_i) \quad (1)$$

where the PMF notation  $f_Y(y) = P(\{Y = y\})$  is abbreviated as  $p(Y)$  (for more details, see Section III).

From the evidence  $E_i(k)$ , the target classification can be obtained by one of several approaches, including the maximum *a posteriori* (MAP) rule, the maximum likelihood estimate, and the Neyman–Pearson rule [7]. To allow for Bayesian updates, the approach presented in this article adopts MAP classification, and the posterior PMF is used to quantify the classification confidence. In particular, given the set of all evidence obtained up to time step  $t_k$ , denoted by  $M_i(k) = \{E_i(1), \dots, E_i(k)\}$ , the CL of the  $i$ th-target’s classification at time  $t_k$  is given by

$$c(Y_i; M_i(k)) \triangleq \max_{y \in \mathcal{Y}} [P(\{Y_i = y\} | M_i(k))]. \quad (2)$$

Then, the desired classification performance can be specified via a CL threshold,  $\varepsilon_{\text{CL}} \in (0, 1)$ , chosen by the user based on the application and the acceptable rates of false alarms. Letting  $T$  denote the total UUV travel time, corresponding to the discrete time step  $K$ , the goal of the path planning algorithm is to achieve a satisfactory CL for all targets in the ROI, or

$$c(Y_i; M_i(K)) \geq \varepsilon_{\text{CL}} \quad \forall i. \quad (3)$$

A higher CL threshold results in lower classification uncertainty and in a larger travel time required to obtain more images of the targets.

In addition to meeting sensing requirements, the path planning approach must also take into account UUV constraints. For example, to minimize the geometric distortions of sonar images, the UUV must be held at a constant speed, altitude, and heading angle with zero roll and pitch angles during every time interval

while sonar data is being recorded [45], [46]. For simplicity, the sonar is assumed to operate at a constant frequency so that the UUV altitude is maintained at a constant value,  $h$ , chosen based on the sensor mode. Then, the UUV configuration can be represented by  $\mathbf{q} = [\mathbf{x} \ \psi]^T$ , where  $\mathbf{x} = [x \ y]^T$ ,  $x$  and  $y$  denote the position of the UUV in  $x_I$  and  $y_I$ , respectively, and  $\psi$  denotes UUV’s heading angle. Then, the target aspect angle is given by  $\varphi = \psi - \theta_{T_i}$  (Fig. 2), and the space of all possible UUV configurations is denoted by  $\mathcal{C}$ . The UUV path is defined by a continuous mapping, denoted by  $\tau : [0, 1] \rightarrow \mathcal{C}$  with  $\tau(0) = \mathbf{q}_{(0)}$  and  $\tau(1) = \mathbf{q}_f$ , where  $\mathbf{q}_{(0)}$  is the given initial configuration and  $\mathbf{q}_f$  is a final configuration to be determined. Thus, the UUV-based sonar planning problem can be summarized as follows.

**Problem 1 (Sensor Path Planning):** Given estimates of  $n$  targets’ positions and orientations  $\mathbf{q}_{T_i}$  for  $i = 1, \dots, n$ , the sensor model (1), the sensor FOV  $\mathcal{S}$ , and the sensor initial configuration  $\mathbf{q}_{(0)}$ , find a path  $\tau$  that minimizes the travel time  $T$  such that the CL constraints (3) are met for all  $n$  targets.

### III. BACKGROUND ON EXPECTED CONFIDENCE LEVEL (ECL)

The information-driven sensor planning approach presented in this article seeks to solve Problem 1 by taking into account the physical properties of the sonar, as well as the ATR process and algorithm. By this approach, the required classification performance can be met while the time and cost associated with operating the UUV-based sonar are minimized. As shown in [7], [10], [11], [40]–[44], the sonar ATR and measurement process can be modeled by a probabilistic sensor model in the form of a joint PMF learned from labeled data. The method adopted from [41], [42] is reviewed here briefly for completeness, but other Bayesian classification methods, such as [4], [5], can be easily incorporated as well.

In underwater sonar imaging, the sensor obtains raw sonar-image matrices that may contain from zero to multiple targets [Fig. 4(a)]. Thus, each raw sonar-image matrix is first processed to recognize all possible targets and, then, segmented to obtain smaller image matrices that each contain only one target, e.g.,

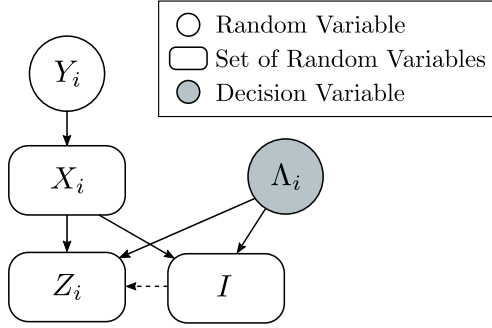


Fig. 5. Probabilistic measurement model for a sonar-imaging sensor. Dashed line represents the feature extraction in the ATR algorithms.

using a matched filter. Let  $t_k$  represent the time at which a target  $i$  is detected in the sonar image and, thus, inside the sensor FOV. From its sonar image segmentation [Fig. 4(b)], a measurement set  $Z_i$  may be obtained as follows. First, raw target features are extracted from each sonar image segmentation, denoted by  $I$ , using a pretrained convolution neural network, *AlexNet* [47]. Subsequently, the set of estimated features,  $\hat{X}_{i1}, \dots, \hat{X}_{if}$ , and inferred classification,  $\hat{Y}_i$ , are obtained using the support vector machine (SVM) proposed in [42], such that  $Z_i = \{\hat{X}_{i1}, \dots, \hat{X}_{if}, \hat{Y}_i\}$  [Fig. 4(b)].

Estimating the CL in consecutive sensor measurement processes requires a probabilistic Bayesian model that captures the influence of sensor mode, environmental conditions, and target features on the hidden target class and observable sensor measurements. The probabilistic sensor model can be defined by a joint PMF, and from the chain rule of probability

$$p(Z_i, X_i, Y_i, \Lambda_i) = p(Z_i | \Lambda_i, X_i, Y_i) p(X_i | \Lambda_i, Y_i) p(Y_i | \Lambda_i) p(\Lambda_i). \quad (4)$$

Because  $\Lambda_i$  is independent of  $X_i$  and  $Y_i$ , and  $p(Z_i | \Lambda_i, X_i, Y_i) = p(Z_i | \Lambda_i, X_i)$ , the probabilistic sensor model is represented by (1). The conditional PMF,  $p(Z_i | \Lambda_i, X_i)$ , is also referred to as a sensor-measurement model. The prior PMFs,  $p(X_i, Y_i)$ ,  $p(Y_i)$ , and  $p(\Lambda_i)$ , can be computed either from the first principle, experiments, or simulation data; if this information is not available, the PMF can be assumed to be uniformly distributed. In this article, the joint PMF is learned from sonar-image data and represented by a Bayesian network model using a directed graph (Fig. 5) and a set of conditional probability tables (CPTs) that can be learned from the labeled data or constructed from the first principle. Target classification is performed based on the MAP rule using the posterior PMF, which can be computed recursively as follows:

$$p(Y_i | M_i(k)) = \frac{p(E_i(k) | Y_i) p(Y_i | M_i(k-1))}{\sum_{Y_i} p(E_i(k) | Y_i) p(Y_i | M_i(k-1))}. \quad (5)$$

The posterior probability of the chosen classification value provides the classification CL as a measure from zero to one of how probable the value is to be correct (where higher probability denotes higher confidence, with one representing certainty).

Because the CL can only be obtained after the image has been processed by the ATR algorithm, this article utilizes the ECL,

defined as the one-step conditional expectation of the CL with respect to the next (future) measurement that would be obtained at a possible sensor configuration. Assuming for simplicity that the environment is homogeneous and the sensor mode is fixed,  $\Lambda_i$  represents all possible UUV viewpoints. Then, based on the evidence set available at  $t_k$ , i.e.,  $M_i(k) = \{E_i(1), \dots, E_i(k)\}$  where  $E_i(k) = \{Z_i(k), \Lambda_i(k)\}$ , the ECL can be obtained as follows:

$$\hat{c}(\Lambda_i(k+1); M_i(k)) = \mathbb{E}_{Z_i(k+1)} \left[ \max_{y \in \mathcal{Y}} P(Y_i = y | M_i(k), E_i(k+1)) \right]. \quad (6)$$

Note that  $\Lambda_i$  is a decision variable, while  $Z_i(k)$  is assumed unknown.

The ECL defined in (6) can be computed using the joint conditional probability, which corresponds to the sensor measurement model. By taking the expectation with respect to  $Z_i$ , (6) can be written by

$$\hat{c}(\Lambda_i(k+1); M_i(k)) = \sum_{Z_i(k+1)} c(Y_i; M_i(k), E_i(k+1)) p(Z_i(k+1) | M_i(k), \Lambda_i(k+1)). \quad (7)$$

The conditional PMF,  $p(Z_i(k+1) | m_i(k), \Lambda_i(k+1))$ , is calculated by marginalizing the joint probability from the sensor-measurement model over the unknown target class  $Y_i$

$$p(Z_i(k+1) | M_i(k), \Lambda_i(k+1)) = \sum_{Y_i} p(Z_i(k+1) | Y_i, \Lambda_i(k+1)) p(Y_i | M_i(k)) \quad (8)$$

where  $p(Z_i(k+1) | Y_i, \Lambda_i(k+1))$  and  $p(Y_i | M_i(k))$  can be obtained from CPTs. Because multiple measurements are necessary for successful target classifications, a series of viewpoint regions must be planned ahead for each target. Denoting the number of planned viewpoint regions of the  $i$ th target by  $n_i$ , the ECL of multiple viewpoint regions can be defined by

$$\hat{c}(\{\Lambda_i(k+1), \dots, \Lambda_i(k+n_i)\}; M_i(k)) = \mathbb{E}_{Z_i(k+1), \dots, Z_i(k+n_i)} \times [c(Y_i; m_i(k), E_i(k+1), \dots, E_i(k+n_i))]. \quad (9)$$

The expectation with respect to a series of  $n_i$  measurements can be computed by recursively updating the ECL for each of  $n_i$  measurement at each time step as the CL is updated recursively (5). The expectation with respect to the measurement at each time step can be computed from (7).

#### IV. INFORMATIVE MULTIVIEW PLANNING

The nature of acoustic wave propagation processes is such that the sonar position and orientation relative to the target of interest (TOI) greatly influence the quality of the measurements and, thus, in turn the information value of sonar imagery produced by the signal processing algorithm. Other sensors, such as synthetic aperture radar as well as imaging sensors in the IR and visible spectrum, are similarly influenced by the relative position and

aspect angle. As a result, directional sensors are often required to obtain images of the same target from different viewpoints, to improve the confidence of the classification and feature estimation algorithms. Furthermore, in the presence of multiple targets, prior information about their approximate location can, in principle, be used to maximize the number of targets in each image as well as to minimize the distance traveled by the UUV.

The approach developed in this article takes into account the UUV configuration, the sensor FOV geometry, and estimates of target positions and orientations by mapping the unions of the targets and sensor-FOV geometries onto the UUV configuration space thus obtaining a so-called C-target (Section IV-A). Then, the most valuable viewpoints are determined by considering their ECL based on the probabilistic measurement model described in Section III (taken from [41]). The approach not only ensures that along the chosen path the targets lie inside the bounded FOV but also determines an efficient path that observes multiple targets for a single pass and reduces travel time by solving a TSP that minimizes distance between the viewpoints required to meet the CL threshold (Section IV-B).

#### A. C-Target Definition and Construction

The region known as C-target represents a subset of the UUV configuration space  $\mathcal{C}$  that enables target measurements, i.e.,  $\mathcal{S} \cap \mathcal{T}_i \neq \emptyset$  [40], [44]. When the target geometry  $\mathcal{T}_i$  is unknown, the target can be reduced to a point and its state estimate can be used to construct a C-target according to the following definition.

*Definition 1 (C-Target):* The  $i$ th target with its state  $\mathbf{q}_{T_i} = [\mathbf{x}_{T_i}^T \theta_{T_i}]^T$  maps in the configuration space,  $\mathcal{C}$ , to the C-target region defined by

$$\mathcal{CT}_i \triangleq \{\mathbf{q} \in \mathcal{C} \mid [\mathbf{x}_{T_i}^T \ 0]^T \in \mathcal{S}(\mathbf{q})\}. \quad (10)$$

From the sidescan sonar FOV geometry, the C-target can be derived in closed form as follows. Let  $r_{\min} \in \mathbb{R}_{\geq 0}$  and  $r_{\max} \in \mathbb{R}_{> 0}$  denote the minimum and maximum distances at which a measurement can be obtained, for a known sensor range  $\mathcal{D} = (r_{\min}, r_{\max})$ . Because the sonar is installed on a mobile UUV, the FOV geometry is a function of the UUV configuration,  $\mathbf{q} = [x \ y \ \theta]^T$ , and for a sidescan sonar can be approximated by two line segments perpendicular to the vehicle heading:

$$\mathcal{S}(\mathbf{q}) = \left\{ \mathbf{p} \in \mathcal{W} \mid \mathbf{p} = \begin{bmatrix} x \\ y \\ 0 \end{bmatrix} \pm \begin{bmatrix} r \cos(\psi + \frac{\pi}{2}) \\ r \sin(\psi + \frac{\pi}{2}) \\ 0 \end{bmatrix}, r \in \mathcal{D} \right\}. \quad (11)$$

Now apply Definition 1 to obtain the C-target corresponding to target  $i$ , i.e.,

$$\mathcal{CT}_i = \left\{ \mathbf{q} \in \mathcal{C} \mid \mathbf{q} = \mathbf{q}_{T_i} \pm \begin{bmatrix} r \cos(\varphi + \theta_{T_i} + \frac{\pi}{2}) \\ r \sin(\varphi + \theta_{T_i} + \frac{\pi}{2}) \\ \varphi \end{bmatrix}, r \in \mathcal{D}, \varphi \in \mathbb{S}^1 \right\} \quad (12)$$

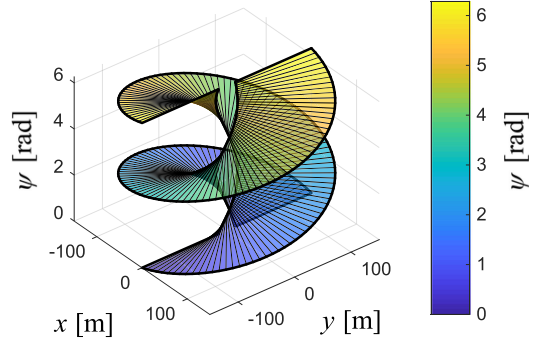


Fig. 6. C-target geometry of a target at  $\mathbf{q}_i = [0 \ 0 \ 0]^T$  observed by a sidescan sonar with ranges  $r_{\min} = 15$  and  $r_{\max} = 150$ .

where  $\mathbb{S}^1$  is a 1-D manifold or *circle*

$$\mathbb{S}^1 = \{(x, y) \mid x^2 + y^2 = 1\}. \quad (13)$$

For an easier visualization and implementation of planning algorithms,  $[0, 2\pi)$  can replace  $\mathbb{S}^1$  using a quotient space,  $[0, 2\pi]/\sim$ , in which the identification declares that 0 and  $2\pi$  are equivalent, denoted by  $0 \sim 2\pi$ . This quotient space homeomorphic to  $\mathbb{S}^1$  “glues” 0 and  $2\pi$  of  $[0, 2\pi]$ , i.e., the value of  $\varphi \in \mathbb{S}$  runs from 0 up to  $2\pi$  and then “wrap around” to 0 [48]. An example geometry of  $\mathcal{CT}_i$  is shown in Fig. 6, where parameters  $r$  and  $\varphi$  represent the sonar distance from the target and the aspect angle, respectively.

Because the aspect angle  $\psi \in \mathbb{S}^1$  wraps around every  $2\pi$ , the geometry of  $\mathcal{CT}_i$  in  $\mathcal{C} \subset \mathbb{R}^2 \times \mathbb{S}^1$  can be considered as a generalized helicoid in  $\mathbb{R}^3$ , defined in [49] as follows.

*Definition 2 (Generalized Helicoid):* Let  $\Pi$  be a plane in  $\mathbb{R}^3$ ,  $l$  be a line in  $\Pi$ , and  $\mathcal{C}$  be a point set in  $\Pi$ . Suppose  $\mathcal{C}$  is rotated in  $\mathbb{R}^3$  about  $l$  and simultaneously displaced parallel to  $l$  so that the speed of displacement is proportional to the speed of rotation, also called *screw motion*. Then, the resulting point set  $\mathcal{M}(\mathcal{C}, c)$  is called the *generalized helicoid* generated by  $\mathcal{C}$ , also called the *profile curve* of  $\mathcal{M}$ . The line  $l$  is called the *axis* of  $\mathcal{M}$ . The ratio of the speed of displacement to the speed of rotation is called *slant* of  $\mathcal{M}$  and is denoted by  $c$ .

Now, adopting Definition 2, the geometry of the  $i$ th C-target,  $\mathcal{CT}_i$ , corresponds to a generalized helicoid  $\mathcal{M}(\mathcal{C}_i, 1)$ , which is generated by the point set

$$\mathcal{C}_i = \{\mathbf{q} \in \mathcal{C} \mid \mathbf{q} = \mathbf{q}_{T_i} \pm [0 \ r \ 0]^T, r \in \mathcal{D}\} \quad (14)$$

on the plane

$$\begin{aligned} \Pi_i = \{[x \ y \ \psi]^T \in \mathcal{C} \mid \cos(x - x_{T_i}) \\ + \sin(y - y_{T_i}) = 0, \psi \in \mathbb{S}\} \end{aligned} \quad (15)$$

by applying the screw motion to the line (axis)

$$l_i = \{[x \ y \ \psi]^T \in \mathcal{C} \mid x = x_{T_i}, y = y_{T_i}, \psi \in \mathbb{S}\} \quad (16)$$

with slant  $c = 1$ .

To transcribe the sensor planning problem (Problem 1) into a TSP, the relative UUV configuration is first discretized and, then, treated as the sensor operating condition ( $\Lambda_i$ ) in the sensor

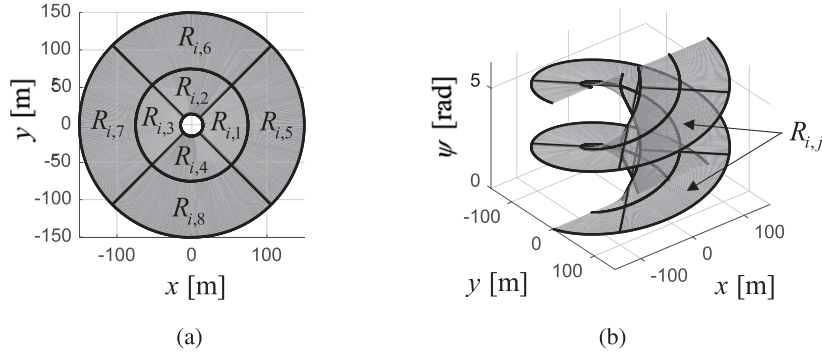


Fig. 7. (a) Top view and (b) isometric view of a partitioned C-target and corresponding viewpoint-regions geometries.

measurement model (Section III). This is accomplished by partitioning each C-target,  $\mathcal{CT}_i$  ( $i = 1, \dots, n$ ), into  $M$  regions by uniformly discretizing the heading angle interval,  $[0, 2\pi)$ , and the sensor range,  $\mathcal{D}$ , as exemplified in Fig. 7. This approximation is useful because it reduces the computational complexity of the planning problem while maintaining sensing efficiency since similar values of  $r$  and  $\varphi$  yield similar measurements. Other helicoid partitioning methods can also be applied, as explained in [50]. A partition of  $\mathcal{CT}_i$  is a pairwise disjoint family

$$\mathcal{V}_i = \{R_{i,j} \mid j \in \{1, \dots, M\}\} \quad (17)$$

such that

$$\bigcup_{j \in \{1, \dots, M\}} R_{i,j} = \mathcal{CT}_i. \quad (18)$$

Each element in  $\mathcal{V}_i$  is referred to a *viewpoint region* in this article. A viewpoint region,  $R_{i,j} \subset \mathcal{CT}_i$ , is a set of points that comprises two disjoint and congruent annular sectors in  $\mathcal{CT}_i$  (Fig. 7). Since  $\mathcal{CT}_i$  is periodic in  $\psi = \pi$ , one annular sector can be defined by translating another by a distance  $\psi = \pi$ .

### B. Formulation of Generalized TSP

A traditional approach to classifying multiple targets is to obtain measurements until the CL exceeds the desired threshold  $\varepsilon_{\text{CL}}$  for each target, as shown in (3). Similarly, a threshold for the ECL,  $\hat{\varepsilon}_{\text{CL}}$ , can be chosen by the user and, then, used to downselect multiple viewpoint regions from the set  $\mathcal{V}_i$ , until the ECL exceeds  $\hat{\varepsilon}_{\text{CL}}$ . Assuming the targets are independent, i.e., the features and classification of one target are independent of those of the other targets in the ROI, this downselected set of viewpoint regions or *neighborhoods*,  $\mathcal{R}_i \subset \mathcal{V}_i$ , can be obtained for every target independently and in any order. Then, a UUV path that visits every region  $\mathcal{R}_i$  ( $i = 1, \dots, n$ ), guarantees that a sufficient number of images is obtained from every target in the sense that

$$\hat{c}(\mathcal{R}_i; M(k)) > \hat{\varepsilon}_{\text{CL}} \quad \forall i. \quad (19)$$

In addition, the solution to Problem 1 can be found by computing the shortest path between the  $n$  viewpoint regions.

The geometry of each neighborhood consists of the two congruent annular sectors defined in Section IV-A. Multiple

neighborhoods intersect at UUV configurations that enable measurements from multiple targets. Under these properties and assumptions, the shortest UUV path visiting all of the target neighborhoods can be found by solving the following generalized TSP.

*Problem 2 [Generalized Traveling Salesman Problem with Neighborhoods (GTSPN)]:* Define  $R_\ell$  by a viewpoint region that the GTSPN path must visit, i.e.,  $R_\ell \in \bigcup_{i=1}^n \mathcal{R}_i$ . Given a set of  $m$  neighborhoods

$$\mathcal{R} = \left\{ R_\ell : R_\ell \in \bigcup_{i=1}^n \mathcal{R}_i, \ell = 1, \dots, m \right\} \quad (20)$$

find the minimum-time path that visits each neighborhood starting at the initial UUV configuration  $\mathbf{q}_{(0)} \in \mathcal{C}$ .

The solution of Problem 2 provides an optimal sensor path able to classify all  $n$  targets in the ROI within a required expected classification CL, in minimum time (assuming UUV travels at a constant speed). This GTSP problem seeks to find the shortest path that visits every neighborhood in a possibly disjoint set at least once. Because an exact GTSPN solution is not available, the following section presents an algorithm for finding an approximate solution to Problem 2.

### V. APPROXIMATE SOLUTION OF GTSPN PROBLEM WITH INTERSECTING NEIGHBORHOODS

Generalized forms of TSPs arise in many robot path planning and sensor coverage problems requiring the minimization of time and energy consumption (e.g., [13], [14] and references therein). Unlike traditional TSP formulations, in which an agent must visit every node in a graph or every point in a Euclidian space, in GTSPs (Fig. 8) the agent must visit any point in each (continuous) neighborhood or in each discrete set of points at least once [51], [52]. In a GTSP, also known as *group TSP* [21] or *one-of-a-set TSP* [53], one seeks to find the shortest tour that visits all of the predefined subsets of points at least once. In a TSP with neighborhoods (TSPN), one seeks the shortest tour that intersects every continuous region at least once.

As formulated in Problem 2, the UUV-based sonar path planning problem corresponds to a GTSPN, because one seeks to find the shortest tour that visits every neighborhood at least once, but each neighborhood consists of multiple (non-Euclidean)

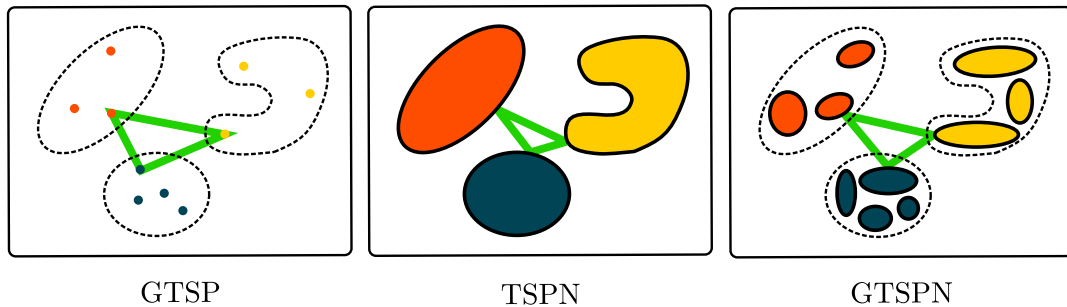


Fig. 8. Graphical representations for the GTSP, TSPN, and GTSPN.

regions [54]. In particular, the neighborhoods in Problem 2 are each comprised of two disjoint continuous regions in the UUV configuration space:

*Problem 3 (GTSPN in Configuration Space):* Find the shortest tour that visits every neighborhood in the set  $\mathcal{R} = \{R_1, \dots, R_m\}$ , comprised of  $n_\iota$  disjoint continuous regions, i.e.,

$$R_\iota = \{S_{\iota,\xi} : S_{\iota,\xi} \subset \mathcal{C}, \xi = 1, \dots, n_\iota\}, \quad \iota = 1, \dots, m. \quad (21)$$

Furthermore, the UUV configuration space is a smooth manifold that is locally like  $\mathbb{R}^3$  but globally different. [55]. Nevertheless, the topology of  $\mathcal{C}$  is the subset topology derived from the Euclidean metric [56, p. 85].

Then, the minimum-time path can be approximated by the shortest path given the assumption of constant UUV speed, and a distance metric can be defined by weighing the translating and rotating motions in the quotient space. GTSPN was first introduced in a Euclidean space in [54] and solved using a hybrid random-key genetic algorithm (HRKGA). The high computational complexity of HRKGA was later reduced using a decoupled algorithm transcribing the GTSPN into a GTSP by first finding the centroid of each region for every neighborhood set and, then, locally adjusting the waypoint locations toward the neighborhood boundaries to improve the solution [57]. A growing self-organizing array algorithm originally proposed in [58] was also applied to GTSPN in [57]. These existing algorithms are not ideally suited to solving Problem 3 because, when selecting waypoints, they do not take into account intersecting neighborhoods, which contain the most valuable configurations because they enable observations from multiple targets. Also, since the UUV path does not necessarily require returning to the initial configuration (tour), it is possible to first sample waypoints and, then, to compute their optimal ordering.

This article presents a new GTSPN solution approach, referred to as IMVP, that is tailored to multiview path planning and, thus, provides a more efficient solution to Problem 3 than existing GTSPN methods. Unlike previous methods, after constructing the  $m$  neighborhoods from the C-targets (as shown in Section IV-A), the IMVP samples the neighborhood intersections using an approximate TSPN algorithm referred to as *TSPN-Intersecting* [59]. The TSPN-Intersecting algorithm uses the *hitting point set*, defined as a set of waypoints from each neighborhood, obtained such that a path connecting the

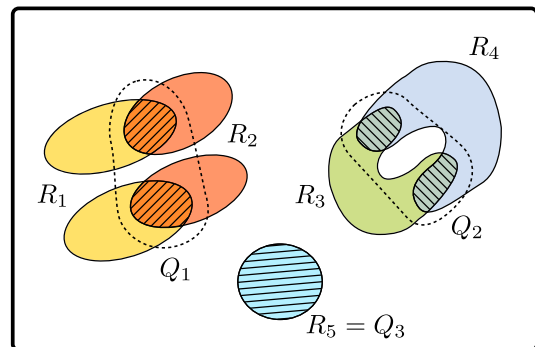


Fig. 9. Minimal disjoint coverage set  $\mathcal{Q} = \{Q_1, Q_2, Q_3\}$  of the set of neighborhoods  $\mathcal{R} = \{R_1, \dots, R_5\}$ .

hitting points intersects every neighborhood. Then, the IMVP approach seeks to sample a minimal number of hitting points by preferentially sampling the neighborhood intersections of highest degree, as follows. A collection of subsets, referred to as *minimal disjoint coverage set*, is defined such that the points sampled from each subset maximize the number of hitting points sampled from the intersection of neighborhoods (Fig. 9).

*Definition 3 (Minimal Disjoint Coverage Set):* A set comprised of a minimum number of regions

$$\mathcal{Q} = \{Q_1, \dots, Q_{m'}\}, \quad m' \leq m \quad (22)$$

is a minimal disjoint coverage set of  $\mathcal{R} = \{R_1, \dots, R_m\}$  if the regions in  $\mathcal{Q}$  are pairwise disjoint, and there exists  $\zeta \in \{1, \dots, m'\}$  such that  $Q_\zeta \subset R_\iota$  for  $\iota = 1, \dots, m$ .

Then, the number of the disjoint regions satisfies  $m' \leq m$ , and the equality holds if the neighborhoods in  $\mathcal{R}$  are disjoint, and  $\mathcal{Q} = \mathcal{R}$ . The heuristic search summarized in Algorithm 1 is developed to compute the minimal disjoint coverage set for a given IMVP neighborhood set,  $\mathcal{R}$ . The heuristic search replaces any two intersecting regions with their mutual intersection for sampling. Each element  $Q_\zeta \in \mathcal{Q}$  may consist of multiple disjoint continuous regions depending on the geometry, position, and orientation of the neighborhoods in  $\mathcal{R}$ . Thus, the hitting pointset is extended to a collection of node sets,  $\mathcal{P} = \{P_1, \dots, P_{m'}\}$ , such that each node set  $P_\zeta \subset Q_\zeta$ , for  $\zeta = 1, \dots, m'$ , consists of points sampled from each disjoint region in  $Q_\zeta$  (Fig. 10). Different rules can be applied for sampling a point from each

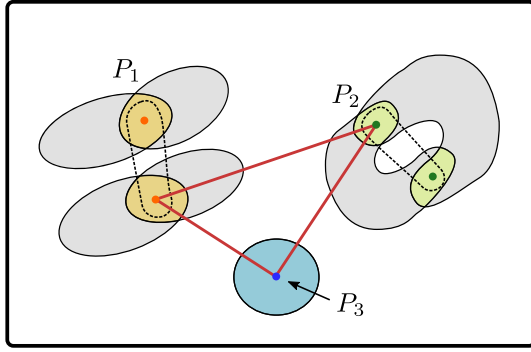


Fig. 10. Collection of nodesets  $\mathcal{P} = \{P_1, P_2, P_3\}$  from the minimal disjoint coverage set  $\mathcal{Q}$  in Fig. 9. The shortest TSP tour is represented by a red line.

---

**Algorithm 1:** Heuristic Search for Minimal Disjoint Coverage Set.

---

**Input:**  $\mathcal{R} = \{R_1, \dots, R_m\}$

**Output:** Minimal disjoint neighborhood set of  $\mathcal{R}$   
initialize  $\mathcal{Q} \leftarrow \mathcal{R}$

**while** every element in  $\mathcal{Q}$  is not pairwise disjoint **do**

**for all** pairs of elements  $Q_i \in \mathcal{Q}$  and  $Q_j \in \mathcal{Q}$  **do**

**if**  $Q_i \cap Q_j \neq \emptyset$  **then**

      replace  $Q_i$  and  $Q_j$  with  $Q_i \cap Q_j$

**end if**

**end for**

**end while**

**return**  $\mathcal{Q}$

---

disjoint region in  $Q_\zeta$ : sampling a centroid if each region in  $Q_\zeta$  is convex; sampling a pole of inaccessibility [60] if regions in  $Q_\zeta$  are not convex; sampling a point on the boundary of each region in  $Q_\zeta$  to obtain a shorter path. As a result, Problem 3 is reduced to a GTSP that seeks the shortest path visiting every node set in a collection  $\mathcal{P} = \{P_1, \dots, P_{m'}\}$ , and, thus, can be solved efficiently as a classical asymmetric TSP using Noon and Bean transformations [61].

The previous sections show how, by considering the constraints and characteristics of the UUV-based imaging sensor, the sensor path planning problem defined in Problem 2 can be reduced to the general GTSPN in Problem 3 and, then, solved as an asymmetric TSP. Now, the geometry of the sensor FOV can be used to further simplify the computation required, as follows. In the case of a sidescan sonar (Fig. 1), each neighborhood consists of two congruent annular sectors (orange sectors in Fig. 11) translated by an angle  $\psi = \pi$ , because of the periodic geometry of the C-target. It can be easily shown that each element  $Q_\zeta$  of the minimal disjoint coverage set  $\mathcal{Q}$  (obtained by Algorithm 1) also consists of a pair of disjoint regions that are congruent and translated by  $\psi = \pi$ . Thus, the projection of  $Q_\zeta$  onto the ROI is comprised of annular sectors, as shown in Fig. 11. To capture not only acoustic highlights but also shadows of targets inside sonar images for the purpose of classification, waypoints are chosen from the centroids (rather than from the boundary) of each region in  $Q_\zeta$ , as illustrated by the blue dots in Fig. 11, providing the

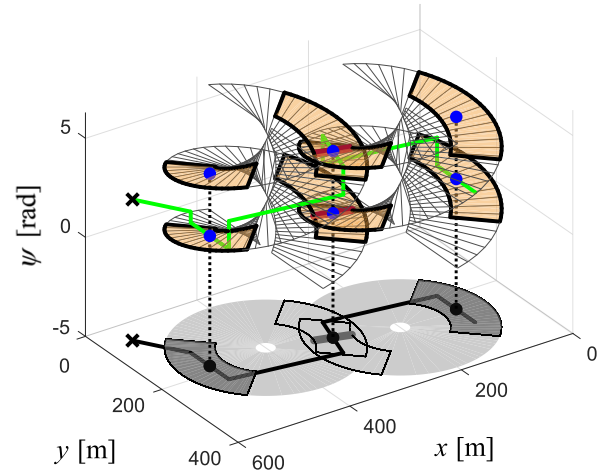


Fig. 11. Illustrative example of shortest path (green solid line) in UUV configuration space obtained by IMVP algorithm for an initial condition (I.C.) symbolized by a black cross, through sampled waypoints symbolized by blue dots.

node set  $P_\zeta \in \mathcal{P}$  ( $\zeta = 1, \dots, m'$ ). To address navigation errors and target uncertainty in real applications, the waypoints can be chosen by directly applying the swath planning approach developed in the MAC algorithm [1]. By applying this approach, a waypoint with the highest detection probability will be chosen by considering the target field as a 2-D Gaussian distribution and by modeling the sensor profile as a function of its range. The sensor profile function can model the degradation of sonar image quality depending on its range, and thus, the quality of sonar images can also be taken into account.

Then, a symmetric TSP is obtained based on the following observations. From the neighborhood geometry, each node set  $P_\zeta$  consists of two UUV configurations characterized by the same position but opposite headings, i.e.,

$$P_\zeta = \{[\mathbf{x}_{(\zeta)}^T \ \psi_{(\zeta,1)}]^T, [\mathbf{x}_{(\zeta)}^T \ \psi_{(\zeta,2)}]^T\}, \quad \zeta = 1, \dots, m' \quad (23)$$

such that

$$|\theta_{(\zeta,1)} - \theta_{(\zeta,2)}| = \pi. \quad (24)$$

The GTSP can be reduced to a symmetric TSP on a Euclidean plane which seeks the shortest path visiting every waypoint position  $\mathbf{x}_{(1)}, \dots, \mathbf{x}_{(m')}$  starting from the given initial UUV configuration,  $\mathbf{q}_{(0)}$ . Then, the shortest path can be computed using Lin–Kernighan heuristic [62] or ant-colony optimization [63], by adding the following two dummy points: 1)  $\mathbf{x}_{d,1}$ , with zero distances to all other points; 2)  $\mathbf{x}_{d,2}$ , with zero distance to  $\mathbf{x}_{d,1}$  and  $\mathbf{q}_{(0)}$ . For simplicity, the two optimal (2-opt) heuristic algorithm [62] is adopted in this article. Subsequently, the path is modified to take account sensor's heading angles and geometric distortions of sonar images by converting each waypoint  $\mathbf{q}_{(\zeta)}$  ( $\zeta = 1, \dots, m'$ ) to a line segment of length  $d$ , i.e.,

$$\tau_{(\zeta)} = \left\{ \mathbf{x} \in \mathbb{R}^2 \mid \mathbf{x} = \mathbf{x}_\zeta + t [\cos \theta_\zeta \ \sin \theta_\zeta]^T, \quad t \in \left[ -\frac{d}{2}, \frac{d}{2} \right] \right\} \quad (25)$$

TABLE I  
INTEGRATED UUV-BASED SONAR SIMULATION VARIABLES AND RESPECTIVE RANGES

Symbol	Nodes	Domain
$Y_i$	Target classification	$\mathcal{Y} = \{0, 1\}$
$X_{i1}$	Target shape feature	$\mathcal{X}_1 = \{\text{sphere, cylinder}\}$
$X_{i2}$	Target volume feature defined by the cube root of target volume [m]	$\mathcal{X}_2 = \{[0, 0.16], [0.16, 0.30], [0.30, 1.1], [1.1, 1.7]\}$
$\mathbf{q}_{T_i}$	Target state	$\mathbb{R}^2 \times \mathbb{S}^1$
$\mathbf{q}$	UUV configuration	$\mathcal{C}$
$\Lambda_i$	Relative UUV configuration at time with respect to the $i$ th target	$\mathcal{V}_i$
$\hat{Y}_i$	Estimated target classification	$\mathcal{Y}$
$\hat{X}_{i1}$	Estimated target shape features	$\mathcal{X}_1$
$\hat{X}_{i2}$	Estimated target volume feature	$\mathcal{X}_2$

where  $d$  is chosen by the user based on the sensor application. Visiting each waypoint through this line segment path ensures that the UUV-based sonar is able to observe targets while traveling along a straight path with constant heading angle, as required for high image quality. Finally, the UUV path can be constructed by choosing the heading angle as  $\theta_{(\zeta,1)}$  or  $\theta_{(\zeta,2)}$ , based on which node sequence results in the shortest path.

## VI. UUV-BASED SONAR SIMULATION ENVIRONMENT AND SEA TEST PREPARATION

### A. UUV-Based Sonar Simulation Environment

The novel IMVP approach presented in this article is first demonstrated on an integrated physics-based simulation of a UUV-based sidescan sonar developed by coauthor Isaacs. In this simulation, the dynamics of the UUV are modeled based on the REMUS 100 autonomous underwater vehicle using six degrees-of-freedom nonlinear equations of motion [64]. A pair of sidescan sonar sensors mounted on the UUV are simulated by generating images obtained from the sensor FOV by beamforming the time domain signals using  $\omega - k$  beamforming [65]. Other beamforming techniques, such as time-delay and chirp scaling, can also potentially be utilized [66]. As can be seen in Fig. 14, objects of interest exhibit strong highlights with varying shadows depths that, while not necessarily unique to objects of interest, provide information about the object features and class. After the image is generated by traveling along a straight line,  $l = 3$  m, the ATR algorithm described in Section III, taken from [42], is used to classify objects that have been detected in sonar imagery and to distinguish them from clutter and seafloor ripples.

The simulated sonar FOV geometry is characterized by the minimum and maximum ranges  $r_{\min} = 15$  m and  $r_{\max} = 150$  m, respectively. Once the UUV trajectory is planned by the IMVP approach, the UUV motion is controlled by a proportional-integral-derivative controller that determines the UUV stern angle, rudder angle, and propeller revolution per minute for accurate trajectory following. For simplicity, in this article,

it is assumed that the UUV position and the target information are provided relative to the inertial frame  $\mathcal{F}_W$ , inside an ROI  $\mathcal{W} = [-L, L] \times [-L, L] \times [0, H]$ , where  $L = 1200$  m and  $H = 50$  m. A target field is generated by sampling a database of underwater objects with the characteristics summarized in Table I and by distributing the objects in the ROI randomly and uniformly, or in random clusters that replicate real-world object fields. Each underwater object may be classified as a TOI,  $y_i = 1$ , or clutter,  $y_i = 0$ , based on its features. As shown in Table I, target features available in the sonar simulation are shape ( $X_{i1}$ ) and volume ( $X_{i2}$ ), i.e.,  $X_i = \{X_{i1}, X_{i2}\}$ .

From the target features estimated from the sonar imagery, denoted by  $Z_i = \{\hat{X}_{i1}, \hat{X}_{i2}\}$ , the class of the  $i$ th object,  $\hat{Y}_i$ , is inferred using the measurement model provided by the joint PMF in Section II, learned from a training database of 260 objects using the ATR approach in [42]. A different database comprised of 260 objects, randomly sampled from the simulation database and not included in the training database, is then used to generate the target fields for the simulated ROI and, subsequently, for testing the path planning algorithms presented in this article. Three classification sets of increasing difficulty are used in this article. The first classification set, labeled as Set A, contains objects that can be classified as TOIs based solely on their volume. The second classification set, labeled as Set B, contains objects that can be classified as TOIs based on both their volume and their shape. The third classification set, labeled as Set C, consists of the same objects as Set B but is characterized by harsher simulated environmental conditions.

### B. Autonomous Vehicle Architecture

As part of the sea-test preparation, the IMVP algorithm was implemented as a standalone C++ library and integrated within the AVA known as AVA. AVA is a software framework initially developed at the Naval Surface Warfare Center Panama City Division (NSWC PCD) to simplify S&T development and reduce the recreation of software year by year for research projects [67]. AVA is structured in three layers to provide a balanced level of individual control: High-level mission and sortie management,

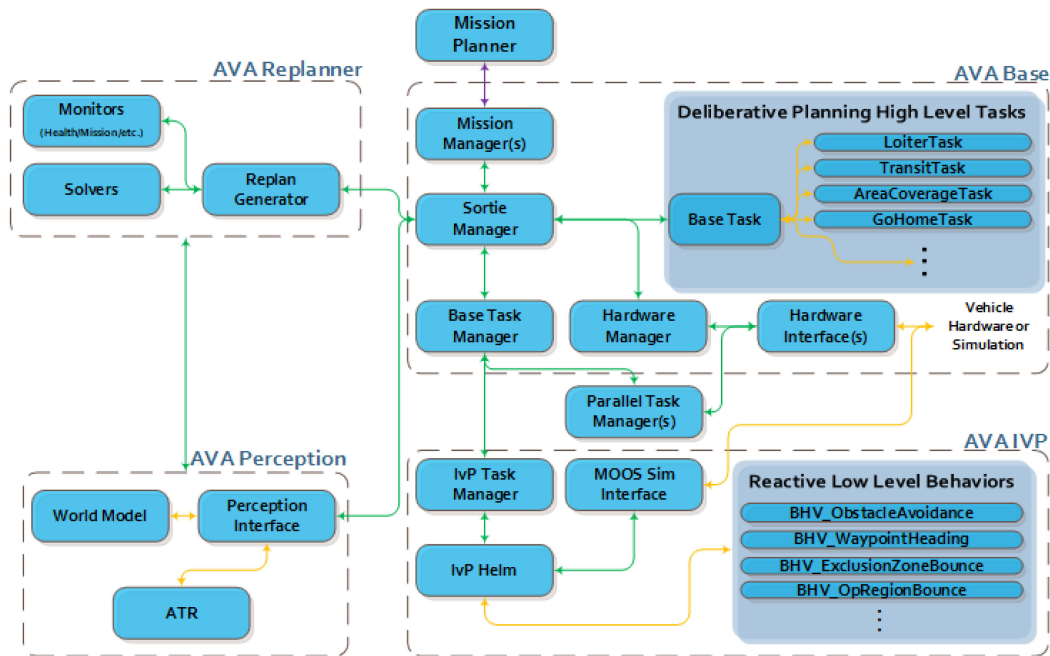


Fig. 12. AVA framework for seatest preparation.

intermediate task layer with deliberative planning capabilities, and low-level behavior planner for reactive capabilities. Additionally, AVA has functions that provide replanning through levels of monitors and solvers while also interacting with perception modules such as world models or automated target recognition software. A layout of the framework for AVA is provided in Fig. 12.

AVA was originally built using the mission oriented operating suite interval programming (MOOS-IvP) environment as a base communication layer while also taking advantage of the low-level behavior components of IvPHelm. Over the past few years, all components of AVA have moved to the robot operating system (ROS) 2.0 for the myriad of advantages the new environment provides. Additionally, IvPHelm and other relevant components of MOOS-IvP have also been converted to ROS 2.0 environment under a similarly named ROS-IvP [68]. These components have greatly been improved since their first iteration into the ROS 1.0 environment.

Using the aforementioned tools as well as other open source tools, AVA works to follow the modular open system approach for components by providing a general framework for communicating between components and multiple base classes that will provide general functionality for new components (tasks, behaviors, etc.). Software is made to simplify the addition of new components and have minimal impact on the architecture. The architecture is created to be platform agnostic and has been demonstrated on several unmanned vehicles across multiple domains (undersea, surface, and ground). AVA is also configured to be third party behavior agnostic, having developed multiple interfaces in the past to collaborate and work with software environment such as operating in parallel with other autonomy architectures, such as SeeByte's Neptune, International Partners, etc.

## VII. IMVP PERFORMANCE RESULTS

The IMVP approach developed in this article is tested on a variety of target fields and compared to the state-of-the-art multiview planning methods known as MAC and clustered MAC (CMAC) [1], [2], [38], [69], [70]. Because the objects' locations and features used for classification all influence the UUV-based sensor performance, the IMVP approach is demonstrated first by considering different object layouts (Section VII-A) and, then, different classification sets (Section VII-B) using the simulation environment described in Section VI. The computational complexity of the IMVP solution algorithm proposed in Section V is analyzed in Section VII-C.

The IMVP performance is evaluated based on the following metrics:

- 1) the travel time ( $T$ ) required to classify all targets with a minimum CL,  $\epsilon_{CL}$ ;
- 2) the total number of contacts ( $N$ ) per travel time;
- 3) the average CL of the targets of interest classified along the path.

Unlike existing multiview planning methods, which take into account only the location of the targets, IMVP seeks to minimize the travel time and images processed by the sensor by selecting only the most informative views. To demonstrate that the desired classification confidence is met by the IMVP planner, the actual CL of all TOIs in the ROI is evaluated by the ATR algorithm (Section III) and, then, averaged as follows:

$$\bar{c}_T = \frac{1}{n'} \sum_{\{i | y_i=1\}} c(Y_i; M_i(K)). \quad (26)$$

Because the CL threshold ( $\epsilon_{CL}$ ) is only required for TOIs, the average is taken over the total number of TOIs in the region ( $n'$ ), not including clutter.

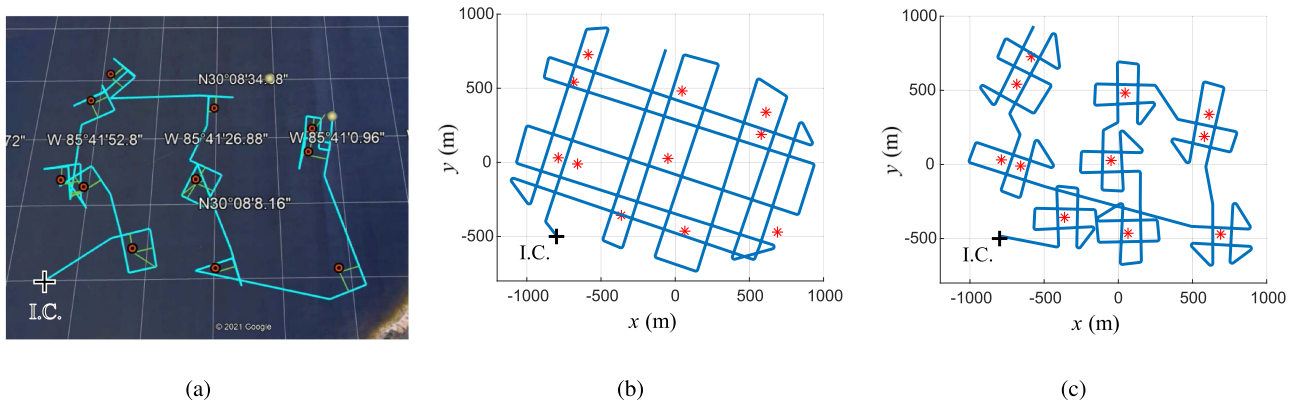


Fig. 13. Path planning results obtained by the (a) IMVP, (b) MAC, and (c) CMAC algorithms for a representative example of target field with classification features drawn from Set B and object locations sampled from a uniform distribution (red stars), where the I.C. of the UUV-based sonar is denoted by the black cross.

The IMVP classification performance is also evaluated by assessing CA, false-alarm ratio (FA), and missed-detection ratio (MD). CA, also known as true positive rate, is defined as the ratio of the number of correctly classified TOIs over total number of TOIs ( $n'$ ). FA is defined as the total number of objects incorrectly classified as TOI over the total number of objects ( $n$ ). The MD or false negative rate is defined as the total number of TOIs incorrectly classified as clutter over  $n$ . The CA per travel time, referred to here as *classification efficiency*, is also evaluated and denoted by  $\eta = CA/T$ .

In the following sections, the IMVP performance is demonstrated for a variety of target fields characterized by different layouts (Section VII-A) and classification features (Section VII-B). In every case study, the IMVP performance is compared to the MAC algorithm, which plans the shortest multiview path to cover every object using a fixed preplanned number of aspect angles, such that every object is detected at least once from each aspect angle [1], [38], [69], [70]. The MAC path may be inefficient for sparse object layouts, requiring the UUV-based sensor to travel long times without observing any objects [1], [38], [69], [70]. The modification proposed in [2], known as CMAC, overcomes this limitation by designing the path based on the size of object clusters that may occur in applications with man-made TOIs [71], [72]. Objects are first grouped in clusters by using density-based spatial clustering of applications with noise method and, then, the shortest path between clusters is found, typically reducing travel time compared to MAC solutions.

As part of the collaboration with NSWC PCD, the IMVP algorithm is integrated and simulated within the AVA architecture before the sea tests (Section VI). A single new task is introduced into AVA that allows for a new reacquire and identify function to be added to the UUV missions. This integration provides both a test case for quickly integrating new functionality into the AVA environment, while also providing real world simulation and in-water testing of the IMVP algorithms. The simulations of the IMVP algorithm within the AVA architecture are performed only for the test cases in Section VII-A due to vehicle issues and available in-water testing time. During the situations where

the vehicle are having issues, the algorithm is operating as required and simply does not result in a complete resultant dataset.

#### A. Influence of Object Location on IMVP Performance

Previous multiview planning studies showed that path performance depends strongly on the object layout [1], [2], [38], [69], [70]. In particular, algorithms that perform well for objects uniformly distributed spatially, at random, over the ROI may not perform adequately when objects are laid out into clusters, and viceversa. In this section, the features of the IMVP algorithm are demonstrated using two case studies with relatively small target fields obtained by sampling the same classification Set B to obtain  $n = 12$  underwater objects, with  $n' = 4$  TOIs. The integrated UUV-based sonar and ATR simulation (Section VI) is then used to evaluate all performance metrics after the UUV's trajectory is executed. The paths computed by the IMVP algorithm are simulated using a high-fidelity AVA simulator to demonstrate that the path is executable under the UUV dynamics constraints for the sea test (Section VII-D). Larger target fields are used in the following section to investigate the IMVP performance with a statistically significant number of objects.

In the first case study, the target field is generated by placing objects in the ROI by randomly sampling underwater objects from the classification Set B (Section VI) and, then, by placing them in  $\mathcal{W}$  at a position and orientation obtained by sampling a uniform distribution defined over  $\mathcal{W} \times \mathbb{S}^1$ . A representative example of IMVP sensor path is plotted in Fig. 13(a), which is a simulated path from the AVA architecture. By leveraging prior sensor measurements, or evidence  $E_i(0)$  ( $i = 1, \dots, n$ ), the IMVP path is able to minimize distance traveled between multiple swaths per target, as well as to decide and plan the number of swaths based on the target examined. When the MAC and CMAC algorithms are applied to the same target field, the resulting paths are as shown in Fig. 13(b) and (c), respectively. It can be seen that these existing algorithms plan the number of swaths *a priori* and equally for all targets, only based on their locations. As a result, the IMVP approach developed in this

TABLE II  
PATH PLANNING AND CLASSIFICATION PERFORMANCE COMPARISON FOR A UNIFORMLY SAMPLED OBJECT DISTRIBUTION

Performance Metric	Algorithm			Improvement <sup>1</sup>
	IMVP	MAC	CMAC	
Travel time, $T$ [hr]	1.20	2.50	2.49	<b>51.8</b> [%]
Contacts per unit time, $N/T$ [ $\text{min}^{-1}$ ]	0.68	0.22	0.28	<b>140</b> [%]
Classification efficiency, $\eta$ [ $\text{hr}^{-1}$ ]	0.56	0.20	0.29	<b>93</b> [%]
Average TOIs CL	0.99	0.97	0.98	1.0 [%]

The bold entities indicates to stress the improvement of the proposed approach over the existing approaches.

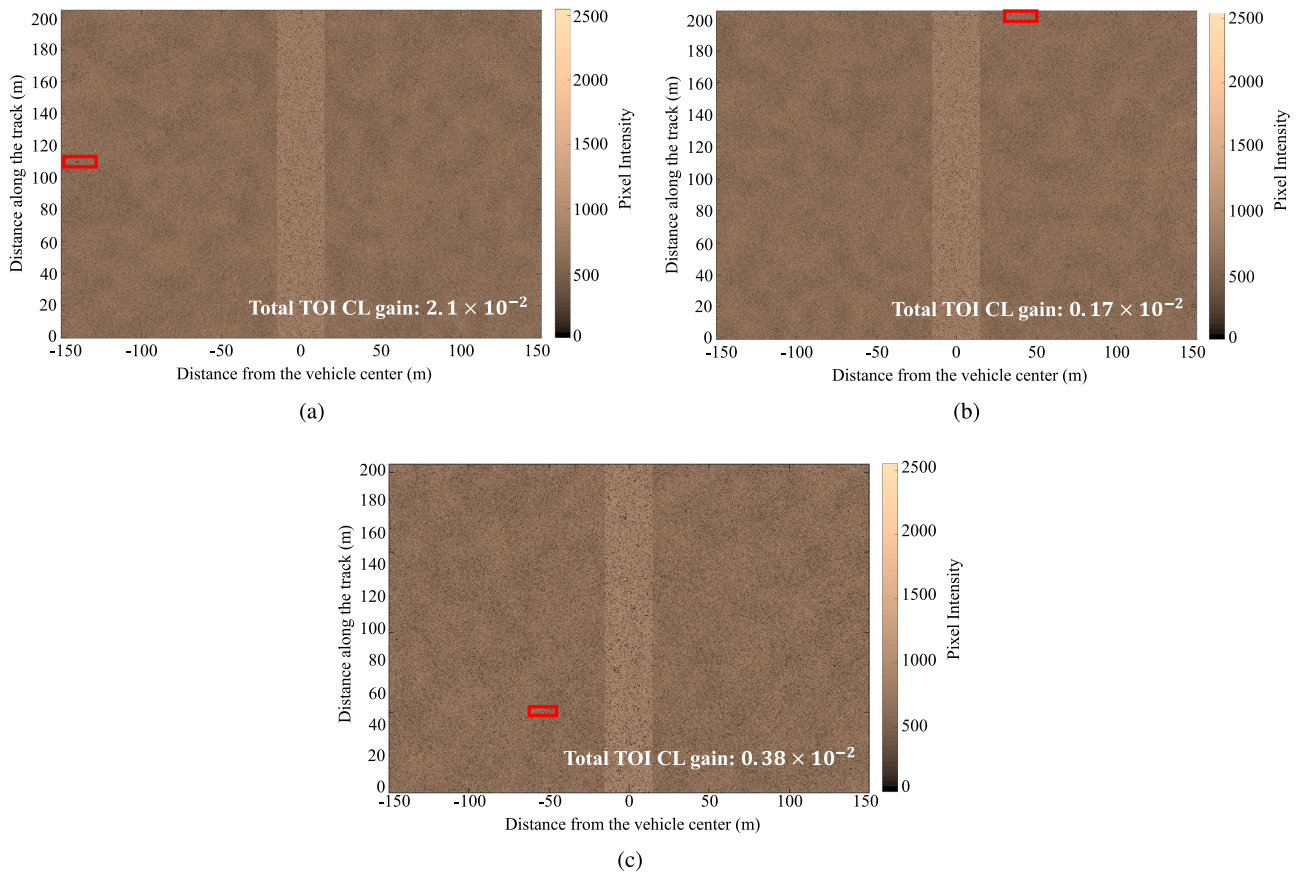


Fig. 14. Sonar images obtained by the (a) IMVP, (b) MAC, and (c) CMAC algorithms around the coordinate  $x = -400$  (m) and  $y = -350$  (m) from the uniform distribution in Fig. 13 and afforded total gain in CL.

article significantly reduces the travel time, while achieving the same required CL for the TOIs (Table II) and the same classification performance reflected in CA, MD, and FA. This is because, while reducing the travel time by approximately 52% compared to the best existing algorithm, the IMVP approach uses prior target information to obtain a large number of high-quality object images (Fig. 14), as demonstrated by the number of contacts and CA per unit time (Table II).

In the second case study, the target field is generated by placing objects in clusters, after randomly sampling underwater objects from the classification Set B (Section VI), using a

uniformly sampled object orientation. Object clusters typically present themselves in applications with man-made TOIs [71], [72] and offer the opportunity to view many objects in a single swatch, provided the optimal aspect angle is planned for the UUV-based sonar. A representative target field with 3 clusters, shown in Fig. 15, is used to compare the trajectories generated by the IMVP, MAC, and CMAC algorithms. As shown by the performance metrics summarized in Table III, the IMVP algorithm obtain images more efficiently by observing multiple targets through a single pass, thus achieving the required TOI CL in less travel time. The CMAC algorithm also exploits the cluster configuration to reduce travel time. However, the IMVP approach is significantly more effective at planning sensor paths

<sup>1</sup>Percent improvement over best existing algorithm.

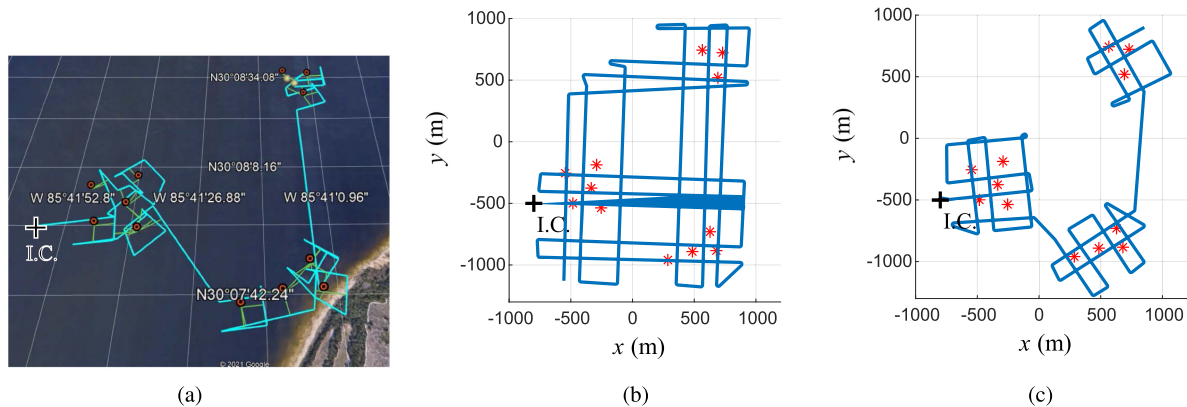


Fig. 15. Path planning results obtained by the (a) IMVP, (b) MAC, and (c) CMAC algorithms for a representative example of target field with classification features drawn from Set B and clustered object locations (red stars), where the I.C. of the UUV-based sonar is denoted by the black cross.

TABLE III  
PATH PLANNING AND CLASSIFICATION PERFORMANCE COMPARISON FOR A CLUSTERED OBJECT DISTRIBUTION

Performance Metric	Algorithm			Improvement <sup>2</sup>
	IMVP	MAC	CMAC	
Travel time, $T$ [hr]	1.63	3.03	1.84	<b>11.4</b> [%]
Contacts per unit time, $N/T$ [ $\text{min}^{-1}$ ]	1.1	0.19	0.34	<b>220</b> [%]
Classification efficiency, $\eta$ [ $\text{hr}^{-1}$ ]	0.69	0.31	0.52	<b>33</b> [%]
Average TOIs CL	0.99	0.95	0.96	3.1 [%]

The bold entities indicates to stress the improvement of the proposed approach over the existing approaches.

that enable multiple detections and utilize the most informative aspect angles, as demonstrated both by the number of object contacts and classification performance per unit time (Table III). This is because the IMVP aspect angles take into consideration the geometry of the C-targets as well as the object features to determine the most informative views and, thus, obtain the most informative sonar images (Fig. 16). As evidenced by these two representative case studies, the IMVP approach is similarly able to determine the optimal path for different object configurations (uniformly distributed or clustered) because of the systematic geometric construction of the C-targets obtained from the sonar FOV geometry and object locations.

### B. Influence of Classification Features on IMVP Performance

In addition to accounting for the sonar FOV geometry and object location, the IMVP approach also provides a systematic methodology for determining the most valuable views based on prior information about the target features and ATR characteristics. The IMVP ability to adapt the path to the complexity of the classification task is demonstrated by using three object classification databases of increasing complexity, referred to as sets A, B, and C, described in Section VI. Using the same set of target locations (Fig. 17), three target fields are generated by sampling  $n = 19$  underwater objects from sets A, B, and C. The corresponding IMVP trajectories, respectively, plotted in

Fig. 17(a)–(c), show that the optimal number of views and the shortest path between them highly depend on the target characteristics. On the other hand, the MAC and CMAC algorithms produce the same identical path for all the three target fields because they only account for the object location (trajectories omitted for brevity). The result is not only a reduced travel time by IMVP but also improved classification efficiency (Table IV), particularly for challenging classification features (set B) and environmental conditions (set C). This is because the IMVP algorithm determines the minimum number of views and the most informative aspect angles required per object, based on its ECL and estimated features, and then determines the shortest path between them.

Finally, a statistically significant analysis of the performance improvement brought about by the IMVP approach compared to existing algorithms is conducted by generating ten target fields for every classification set (set A, B, and C). Every classification performance metric is then evaluated by averaging 1000 trials to obtain both its mean value and standard deviation. In addition to classification efficiency, the actual gain in CL per unit time is computed as follows,

$$\beta = \frac{1}{nT} \sum_{i=1}^n c(Y_i; M_i(K)) \quad (27)$$

in order to determine how informative are the sonar images obtained by the IMVP approach. The mean value and standard deviation of the classification efficiency ( $\eta$ ) and of the CL gain

<sup>2</sup>Percent improvement over best existing algorithm.

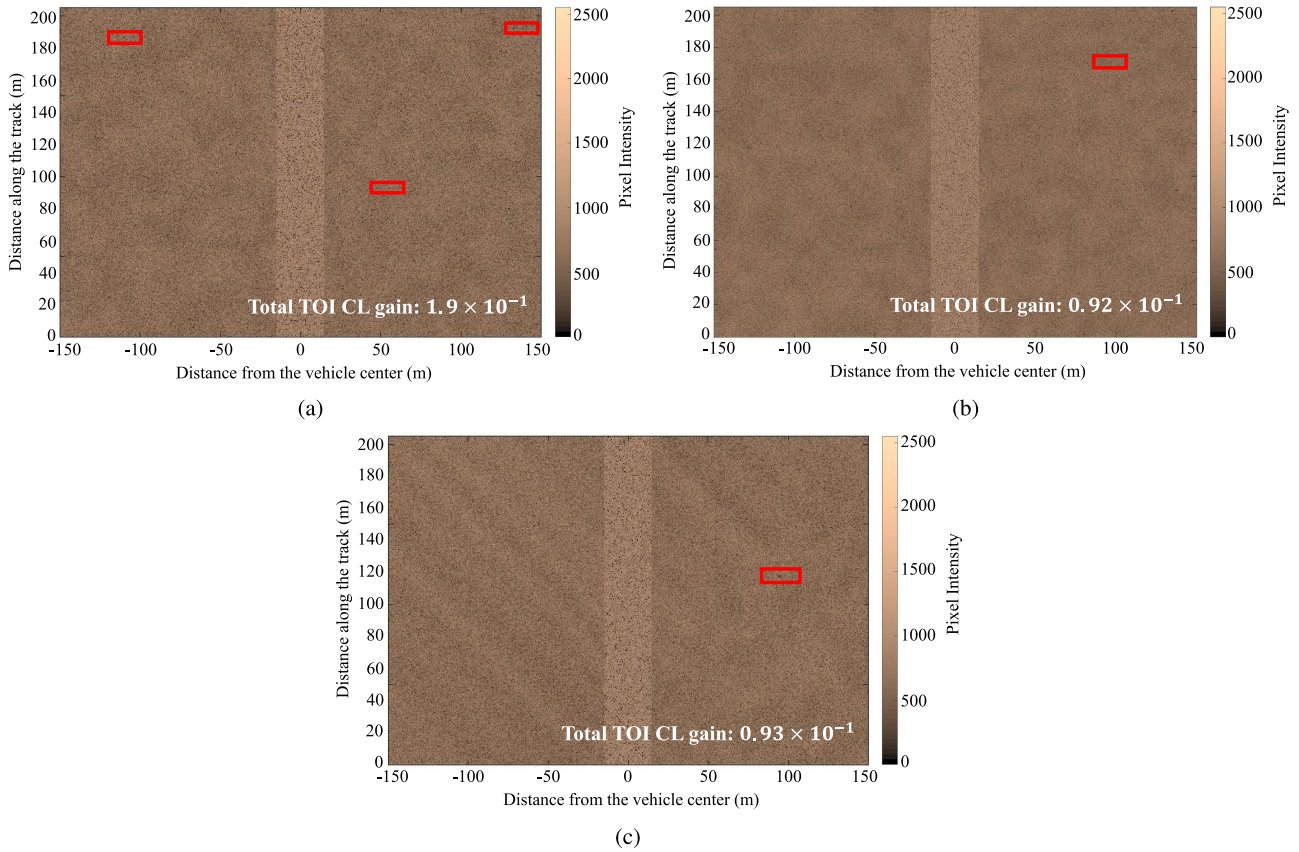


Fig. 16. Sonar images obtained by the (a) IMVP, (b) MAC, and (c) CMAC algorithms around the coordinate  $x = 700$  (m) and  $y = -800$  (m) from the clustered distribution in Fig. 15 and afforded total gain in CL.

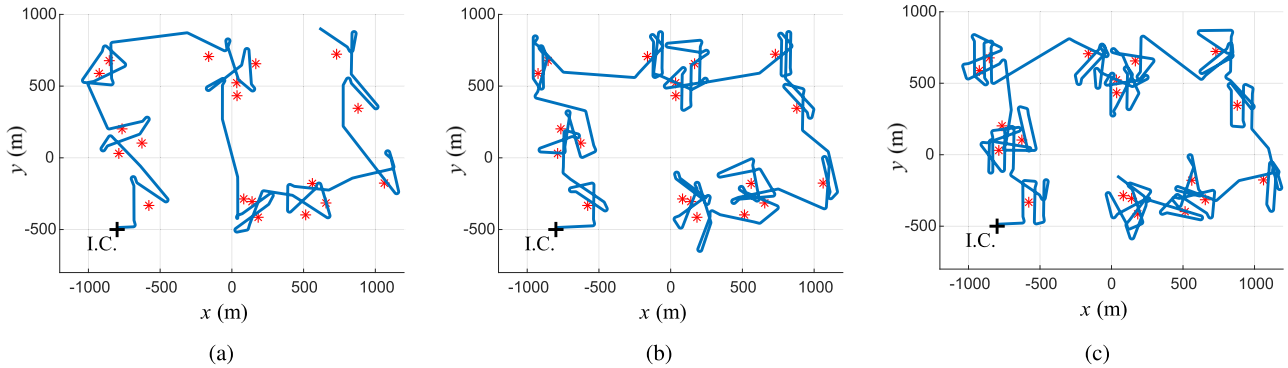


Fig. 17. IMVP path planning results obtained for a fixed set of object locations (red stars) and different object features sampled from classification sets A (a), B (b), and C (c), where the I.C. of the UUV-based sonar is denoted by the black cross.

per unit time ( $\beta$ ) are plotted in Figs. 18 and 19, respectively, for the IMVP approach, as well as for the MAC and CMAC algorithms.

The results in Fig. 18 show not only that the IMVP approach achieves a much higher classification efficiency—namely 88% improvement for set A, 49% improvement for set B, and 13% improvement for set C—but also a much smaller standard deviation than that of MAC and CMAC algorithms, indicating that the IMVP performance is not only higher but also more

robust. Furthermore, the classification results obtained by the IMVP approach also have higher confidence than those provided by the MAC and CMAC algorithms. The results in Fig. 19 show that the IMVP approach results in a much higher CL gain per unit time—namely 91% improvement for set A, 43% improvement for set B, and 18% improvement for set C—as well as in a much smaller standard deviation than that of MAC and CMAC algorithms, indicating that the CL improvement also is more robust.

TABLE IV  
PATH PLANNING AND CLASSIFICATION PERFORMANCE COMPARISON FOR DIFFERENT CLASSIFICATION SETS

Performance Metric	IMVP Performance (Improvement <sup>3</sup> )		
	Set A	Set B	Set C
Travel time, $T$ [hr]	1.67 ( <b>47.7%</b> )	2.51 ( <b>21.6%</b> )	3.14 ( <b>2.10%</b> )
Contacts per unit time, $N/T$ [ $\text{min}^{-1}$ ]	0.59 ( <b>59.0%</b> )	0.80 ( <b>64.2%</b> )	0.67 ( <b>79.8%</b> )
Average CL of TOIs	1.0 (0%)	0.97 (3.7%)	0.96 (6.0%)
Classification efficiency, $\eta$ [ $\text{hr}^{-1}$ ]	0.60 ( <b>91%</b> )	0.37 ( <b>32%</b> )	0.23 ( <b>12%</b> )
Classification Accuracy (CA)	1.0 (0%)	0.93 (3.7%)	0.71 (9.7%)
False Alarm Ratio (FA)	0.0 (0%)	0.038 (9.4%)	0.27 (1.3%)
Missed Detection Ratio (MD)	0.0 (0%)	0.071 (30%)	0.29 (18%)

The bold entities indicates to stress the improvement of the proposed approach over the existing approaches.

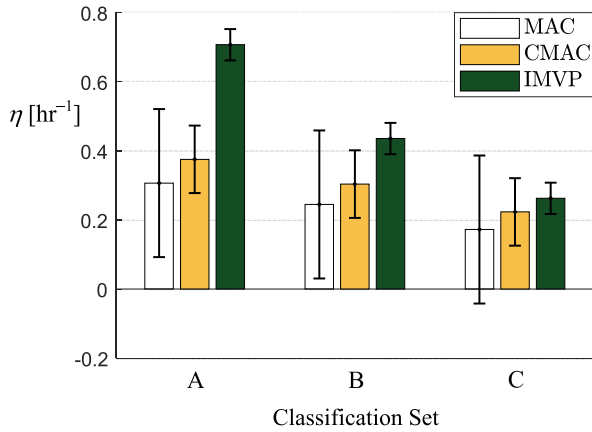


Fig. 18. Classification efficiency mean-value and standard deviation (vertical bars) for IMVP, MAC, and CMAC algorithms.

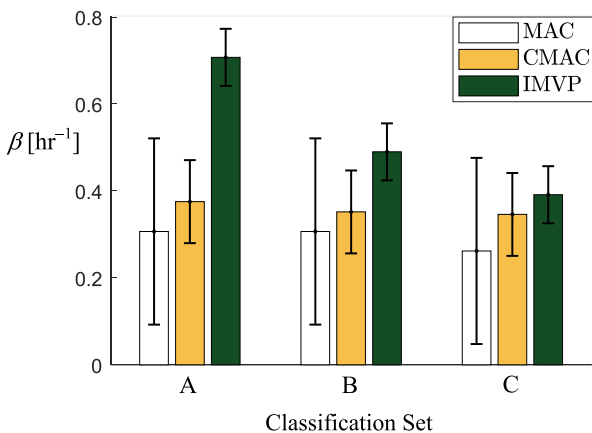


Fig. 19. CL gain per unit time and standard deviation (vertical bars) for IMVP, MAC, and CMAC algorithms.

### C. Computational Complexity Analysis

The IMVP solution algorithm relies on two steps. The first step is to obtain a set  $\mathcal{Q}$  of downselect discretized C-target

regions characterized by satisfactory ECL for every object in the ROI.<sup>3</sup> The second step is to solve a TSPN and produce the shortest path that visits all regions in  $\mathcal{Q}$  at least once. The computational complexity of the first step is lower than  $O(n \cdot 2^M)$ , because checking every possible combinations of C-target regions takes  $\sum_{k=1}^M \binom{M}{k} = 2^M$  time. Let  $L$  denote the number of regions that are downselected from all C-targets. Then, the TSPN solution requires at worst  $O(L^2)$  time. Since the two steps are conducted consecutively, the overall IMVP computational complexity is  $O(n \cdot 2^M) + O(L^2)$ .

The main factor contributing to the IMVP computational complexity is  $2^M$ , a term which derives from evaluating the ECL of every possible combination of discretized C-target regions. This computation can be reduced to  $O(M)$  when the maximum number of downselected regions can be fixed *a priori* as in the CMAC algorithm. Also, the term  $L^2$ , derived from the computation of neighborhood intersections, dictates the highest complexity of the TSPN solution. This computation can be reduced by adopting a greedy solution algorithm that does not consider neighborhood intersections at the expense of travel time optimality.

### D. Sea Test Experimental Results

Sea tests were conducted in collaboration with NSW PCD to demonstrate the feasibility and effectiveness of the IMVP algorithm. The sea trials were performed at Saint Andrew Bay area near Panama City, FL, USA [Fig. 20(a)]. The IMVP planner was first integrated within the AVA architecture (Fig. 12) and, then, executed onboard a REMUS 100 for the test case described in Fig. 13(a). The REMUS trajectory executed during the sea trial is shown in Fig. 20, and the corresponding ATR performance is evaluated using the sonar simulation described in Section VI. The results in Table V show that the sea-test REMUS trajectory and classification performance are similar or better than those obtained by the AVA simulation. The REMUS speed was maintained at approximately 3 m/s, as in the simulation environment (Section VI). The number of target contacts was,

<sup>3</sup>Percent improvement over best existing algorithm.

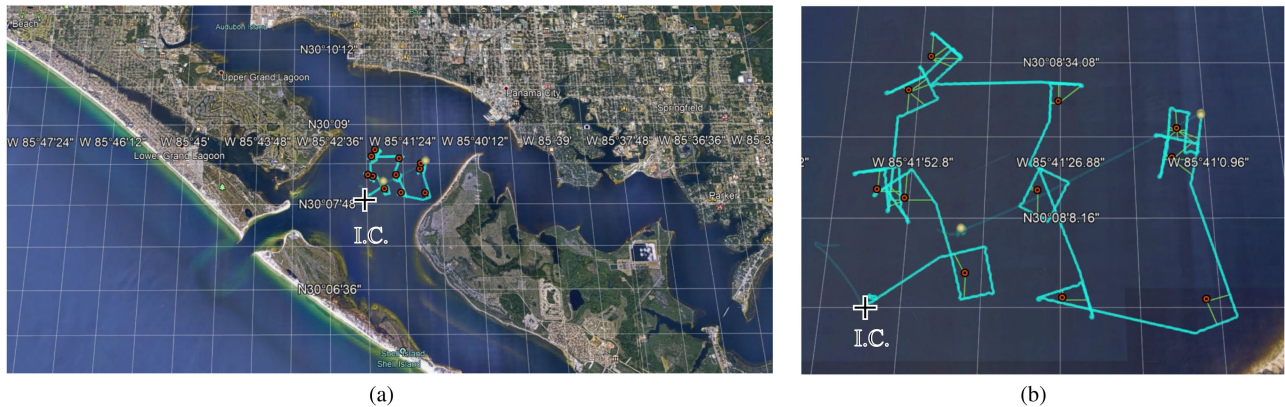


Fig. 20. (a) Bird-eye view of the sea tests in the Saint Andrew Bay area in Panama City, FL, USA. (b) Close view of the REMUS IMVP trajectory executed at sea for the target field described in Fig. 13(a), and a vehicle I.C. denoted by the black cross.

TABLE V  
IMVP ALGORITHM PATH PLANNING AND CLASSIFICATION PERFORMANCE  
COMPARISON FOR SEA TEST AND AVA SIMULATION

Performance Metric	IMVP Algorithm	
	Sea Test	AVA Simulation
Travel time, $T$ [hr]	1.15	1.20
Contacts per unit time, $N/T$ [ $\text{min}^{-1}$ ]	0.59	0.68
Classification efficiency, $\eta$ [ $\text{hr}^{-1}$ ]	0.53	0.56
Average TOIs CL	0.98	0.99

however, reduced from 49 (in AVA simulation) to 40 in the sea test due to disturbance in the yawing motion caused by the sea waves. For the targets acquired, the results in Table V show that the REMUS was able to execute the IMVP path with good accuracy in real undersea environments, thus resulting in similar target classification performance.

## VIII. CONCLUSIONS

This article presents a novel approach to planning sensor measurements and motions in applications that require multiple looks or views per target, such as underwater imaging. The approach, referred to as IMVP, takes into account the sensor FOV geometry and the target position and orientation by constructing a so-called C-target in the mobile sensor's configuration space. By this approach, the expected information value of every possible sensor look (or view) of the target can be quantified systematically as a function of the sensor configuration. The IMVP approach is demonstrated on a UUV-based sidescan sonar that must classify multiple targets with a minimum required CL. As a result, the information value of C-target regions is represented by the ECL derived from prior sensor measurements and ATR model. An approximate algorithm for solving the multiview planning problem, reduced to a GTSPN, is also presented to leverage intersecting C-target regions and maximize the number of targets detected in sonar images. The results obtained from a high-fidelity closed-loop imaging sonar simulation show that IMVP significantly outperforms existing

state-of-the-art multiview planning methods, known as MAC and CMAC algorithms. In fact, IMVP-guided sonar are able to complete multitarget classification tasks with equal or superior classification performance in approximately half the time of existing algorithms.

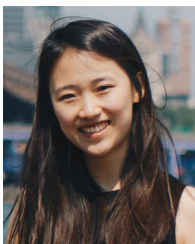
The IMVP approach is shown to adapt the UUV path based on individual target features, the difficulty of classification task, and the configuration of the target field. In real operations, the IMVP method can be reformulated to have a time constraint and to maximize the ECL or information gain for target classification. In this formulation, the IMVP method will vary the number of views for each target to limit the operation time while choosing the most informative viewpoints. When an additional total time constraint is given, the IMVP approach can be modified to limit the number of views by removing the least informative viewpoint. The proposed IMVP approach can also be extended to operate in the online configuration, where the contact reinspection is performed right after the detection. This online approach will plan an additional view based on the ECL until the CL reaches a user-defined threshold. Therefore, the IMVP approach is not only promising for other multiview sensor applications but also for the development of adaptive planning algorithms.

## REFERENCES

- [1] M. J. Bays, A. Shende, D. J. Stilwell, and S. A. Redfield, "Theory and experimental results for the multiple aspect coverage problem," *Ocean Eng.*, vol. 54, pp. 51–60, 2012.
- [2] A. Sriraman and M. J. Bays, "Efficient reacquire and identify path planning over large areas," in *Proc. OCEANS Conf.*, St. John's, NL, Canada, 2014, pp. 1–7.
- [3] M. Couillard, J. Fawcett, and M. Davison, "Optimizing constrained search patterns for remote mine-hunting vehicles," *IEEE J. Ocean. Eng.*, vol. 37, no. 1, pp. 75–84, Jan. 2012.
- [4] G. A. Hollinger, U. Mitra, and G. S. Sukhatme, "Active classification: Theory and application to underwater inspection," in *Proc. 15th Int. Symp. Robot. Res. (ISRR)*, Puerto Varas, Chile, 2017, pp. 95–110.
- [5] N. Palomeras, N. Hurtós, E. Vidal, and M. Carreras, "Autonomous exploration of complex underwater environments using a probabilistic next-best-view planner," *IEEE Robot. Autom. Lett.*, vol. 4, no. 2, pp. 1619–1625, Apr. 2019.
- [6] V. Myers and D. P. Williams, "Adaptive multiview target classification in synthetic aperture sonar images using a partially observable Markov decision process," *IEEE J. Ocean. Eng.*, vol. 37, no. 1, pp. 45–55, Jan. 2012.

- [7] S. Ferrari and T. Wettergren, *Information-Driven Planning and Control*. Cambridge, MA, USA: MIT Press, 2021, pp. 493–564.
- [8] K. A. Baumgartner, S. Ferrari, and A. V. Rao, “Optimal control of an underwater sensor network for cooperative target tracking,” *IEEE J. Ocean. Eng.*, vol. 34, no. 4, pp. 678–697, Oct. 2009.
- [9] C. Cai and S. Ferrari, “Comparison of information-theoretic objective functions for decision support in sensor systems,” in *Proc. IEEE Amer. Control Conf.*, 2007, pp. 3559–3564.
- [10] S. Ferrari and A. Vaghi, “Demining sensor modeling and feature-level fusion by Bayesian networks,” *IEEE Sensors J.*, vol. 6, no. 2, pp. 471–483, Apr. 2006.
- [11] G. Zhang, S. Ferrari, and C. Cai, “A comparison of information functions and search strategies for sensor planning in target classification,” *IEEE Trans. Syst., Man, Cybern. B, Cybern.*, vol. 42, no. 1, pp. 2–16, Feb. 2012.
- [12] H. Wei, P. Zhu, M. Liu, J. P. How, and S. Ferrari, “Automatic pan-tilt camera control for learning dirichlet process Gaussian process (DPGP) mixture models of multiple moving targets,” *IEEE Trans. Autom. Control*, vol. 64, no. 1, pp. 159–173, Jan. 2019.
- [13] S. Alatarsev, S. Stellmacher, and F. Ortmeier, “Robotic task sequencing problem: A survey,” *J. Intell. Robot. Syst.*, vol. 80, no. 2, pp. 279–298, 2015.
- [14] D. G. Macharet and M. F. Campos, “A survey on routing problems and robotic systems,” *Robotica*, vol. 36, no. 12, pp. 1781–1803, 2018.
- [15] A. Dumitrescu and C. D. Tóth, “The traveling salesman problem for lines, balls, and planes,” *ACM Trans. Algorithms*, vol. 12, no. 3, pp. 43:1–43:29, 2016.
- [16] A. Dumitrescu and C. D. Tóth, “Constant-factor approximation for TSP with disks,” 2017, [arXiv:1506.07903v4](https://arxiv.org/abs/1506.07903v4).
- [17] I. O. Bercea, “Improved bounds for the traveling salesman problem with neighborhoods on uniform disks,” 2018, [arXiv:1809.07159](https://arxiv.org/abs/1809.07159).
- [18] J. S. Mitchell, “A PTAS for TSP with neighborhoods among fat regions in the plane,” in *Proc. 18th Annu. ACM-SIAM Symp. Discrete Algorithms (SODA)*, New Orleans, LA, USA, 2007, pp. 11–18.
- [19] J. S. Mitchell, “A constant-factor approximation algorithm for TSP with pairwise-disjoint connected neighborhoods in the plane,” in *Proc. 26th Annu. Symp. Comput. Geometry*, 2010, pp. 183–191.
- [20] T.-H. H. Chan and K. Elbassioni, “A ptas for TSP with fat weakly disjoint neighborhoods in doubling metrics,” *Discrete Comput. Geometry*, vol. 46, no. 4, pp. 704–723, 2011.
- [21] K. Elbassioni, A. V. Fishkin, N. H. Mustafa, and R. Sitters, “Approximation algorithms for Euclidean group TSP,” in *Proc. 32nd Int. Conf. Automata, Lang. Program. (ICALP)*, Lisbon, Portugal, 2005, pp. 1115–1126.
- [22] S. Rahman, A. Q. Li, and I. Rekleitis, “Sonar visual inertial slam of underwater structures,” in *Proc. IEEE Int. Conf. Robot. Autom.*, 2018, pp. 1–7.
- [23] P. Brehmer, T. Lafont, S. Georgakarakos, E. Josse, F. Gerlotto, and C. Collet, “Omnidirectional multibeam sonar monitoring: Applications in fisheries science,” *FISH Fisheries*, vol. 7, no. 3, pp. 165–179, 2006.
- [24] D. J. Walker and J. B. Alford, “Mapping lake sturgeon spawning habitat in the upper tennessee river using side-scan sonar,” *North Amer. J. Fisheries Manage.*, vol. 36, no. 5, pp. 1097–1105, 2016.
- [25] M. Rahnemoonfar, A. F. Rahman, R. J. Kline, and A. Greene, “Automatic seagrass disturbance pattern identification on sonar images,” *IEEE J. Ocean. Eng.*, vol. 44, no. 1, pp. 132–141, Jan. 2019.
- [26] S. Sariel, T. Balch, and N. Erdogan, “Naval mine countermeasure missions,” *IEEE Robot. Autom. Mag.*, vol. 15, no. 1, pp. 45–52, Mar. 2008.
- [27] V. Myers and J. Fawcett, “A template matching procedure for automatic target recognition in synthetic aperture sonar imagery,” *IEEE Signal Process. Lett.*, vol. 17, no. 7, pp. 683–686, Jul. 2010.
- [28] J. C. Isaacs, “Sonar automatic target recognition for underwater UXO remediation,” in *Proc. IEEE Conf. Comput. Vis. Pattern Recognit. Workshops*, 2015, pp. 134–140.
- [29] J. C. Isaacs and A. Srivastava, “Geodesic shape distance and integral invariant shape features for automatic target recognition,” in *Proc. MTS/IEEE OCEANS Conf.*, Seattle, WA, USA, 2010, pp. 1–6.
- [30] D. P. Williams, “Fast target detection in synthetic aperture sonar imagery: A new algorithm and large-scale performance analysis,” *IEEE J. Ocean. Eng.*, vol. 40, no. 1, pp. 71–92, Jan. 2015.
- [31] D. Köhntopp, B. Lehmann, D. Kraus, and A. Birk, “Classification and localization of naval mines with superellipse active contours,” *IEEE J. Ocean. Eng.*, vol. 44, no. 3, pp. 767–782, Jul. 2019.
- [32] R. J. Urick, *Principles of Underwater Sound*. New York, NY, USA: Tata McGraw-Hill Education, 1967, pp. 263–296.
- [33] D. Williams and J. Groen, “Multi-view target classification in synthetic aperture sonar imagery,” in *Proc. Int. Conf. Exhib. Underwater Acoustic Meas.*, 2009, pp. 699–704.
- [34] J. Fawcett, V. Myers, D. Hopkin, A. Crawford, M. Couillard, and B. Zerr, “Multiaspect classification of sidescan sonar images: Four different approaches to fusing single-aspect information,” *IEEE J. Ocean. Eng.*, vol. 35, no. 4, pp. 863–876, Oct. 2010.
- [35] D. P. Williams and S. Dugelay, “Multi-view SAS image classification using deep learning,” in *Proc. MTS/IEEE OCEANS Conf.*, Monterey, CA, USA, 2016, pp. 1–9.
- [36] J. C. Isaacs and J. D. Tucker, “Signal diffusion features for automatic target recognition in synthetic aperture sonar,” in *Proc. Digit. Signal Process. Signal Process. Educ. Meeting*, 2011, pp. 461–465.
- [37] J. C. Isaacs and J. D. Tucker, “Diffusion features for target specific recognition with synthetic aperture sonar raw signals and acoustic color,” in *Proc. IEEE Conf. Comput. Vis. Pattern Recognit. Workshops*, 2011, pp. 27–32.
- [38] M. J. Bays, A. Shende, D. J. Stilwell, and S. A. Redfield, “A solution to the multiple aspect coverage problem,” in *Proc. IEEE Int. Conf. Robot. Autom.*, 2011, pp. 1531–1537.
- [39] R. E. Hansen, “Synthetic aperture sonar technology review,” *Marine Technol. Soc. J.*, vol. 47, no. 5, pp. 117–127, 2013.
- [40] C. Cai and S. Ferrari, “Information-driven sensor path planning by approximate cell decomposition,” *IEEE Trans. Syst., Man, Cybern. B, Cybern.*, vol. 39, no. 3, pp. 672–689, Jun. 2009.
- [41] S. Chang, J. Isaacs, B. Fu, J. Shin, P. Zhu, and S. Ferrari, “Confidence level estimation in multi-target classification problems,” *Proc. SPIE*, vol. 10628, 2018, Art. no. 1062818.
- [42] P. Zhu, J. Isaacs, B. Fu, and S. Ferrari, “Deep learning feature extraction for target recognition and classification in underwater sonar images,” in *Proc. IEEE 56th Annu. Conf. Decis. Control (CDC)*, 2017, pp. 2724–2731, doi: [10.1109/CDC.2017.8264055](https://doi.org/10.1109/CDC.2017.8264055).
- [43] G. Zhang, S. Ferrari, and M. Qian, “An information roadmap method for robotic sensor path planning,” *J. Intell. Robot. Syst.*, vol. 56, no. 1/2, pp. 69–98, 2009.
- [44] W. Lu, G. Zhang, and S. Ferrari, “An information potential approach to integrated sensor path planning and control,” *IEEE Trans. Robot.*, vol. 30, no. 4, pp. 919–934, Aug. 2014.
- [45] D. T. Cobra, A. V. Oppenheim, and J. S. Jaffe, “Geometric distortions in side-scan sonar images: A procedure for their estimation and correction,” *IEEE J. Ocean. Eng.*, vol. 17, no. 3, pp. 252–268, Jul. 1992.
- [46] P. Blondel, *The Handbook of Sidescan Sonar*. Berlin, Germany: Springer, 2010.
- [47] A. Krizhevsky, I. Sutskever, and G. E. Hinton, “Imagenet classification with deep convolutional neural networks,” in *Proc. Adv. Neural Inf. Process. Syst.*, 2012, pp. 1097–1105.
- [48] S. M. LaValle, *Planning Algorithms*. Cambridge, U.K.: Cambridge Univ. Press, 2006.
- [49] E. Abbena, S. Salamon, and A. Gray, *Modern Differential Geometry of Curves and Surfaces With Mathematica*. 3rd ed. Boca Raton, FL, USA: CRC, 2017, pp. 470–473.
- [50] I. Becerra, L. M. Valentín-Coronado, R. Murrieta-Cid, and J.-C. Latombe, “Reliable confirmation of an object identity by a mobile robot: A mixed appearance/localization-driven motion approach,” *Int. J. Robot. Res.*, vol. 35, no. 10, pp. 1207–1233, 2016.
- [51] P. Tokekar, J. VanderD. HookMulla, and V. Isler, “Sensor planning for a symbiotic UAV and UGV system for precision agriculture,” *IEEE Trans. Robot.*, vol. 32, no. 6, pp. 1498–1511, Dec. 2016.
- [52] A. K. Budhiraja, “View point planning for inspecting static and dynamic scenes with multi-robot teams,” Ph.D. dissertation, Dept. Elect. Comput. Eng. Virginia Tech, Blacksburg, VA, USA, 2017.
- [53] J. S. Mitchell *et al.*, “Geometric shortest paths and network optimization,” *Handbook Comput. Geometry*, vol. 334, pp. 633–702, 2000.
- [54] K. Vicencio, B. Davis, and I. Gentilini, “Multi-goal path planning based on the generalized traveling salesman problem with neighborhoods,” in *Proc. IEEE/RSJ Int. Conf. Intell. Robots Syst.*, 2014, pp. 2985–2990.
- [55] J. J. Kuffner, “Effective sampling and distance metrics for 3D rigid body path planning,” in *Proc. IEEE Int. Conf. Robot. Autom.*, 2004, pp. 3993–3998.
- [56] J.-C. Latombe, *Robot Motion Planning*, vol. 124. Berlin, Germany: Springer, 2012.
- [57] J. Faigl, P. Váňa, and J. Deckerová, “Fast heuristics for the 3-D multi-goal path planning based on the generalized traveling salesman problem with neighborhoods,” *IEEE Robot. Autom. Lett.*, vol. 4, no. 3, pp. 2439–2446, Jul. 2019.
- [58] J. Faigl, “GSOA: Growing self-organizing array-unsupervised learning for the close-enough traveling salesman problem and other routing problems,” *Neurocomputing*, vol. 312, pp. 120–134, 2018.

- [59] K. Elbassioni, A. V. Fishkin, and R. Sitters, "Approximation algorithms for the Euclidean traveling salesman problem with discrete and continuous neighborhoods," *Int. J. Comput. Geometry Appl.*, vol. 19, no. 2, pp. 173–193, 2009.
- [60] D. Garcia-Castellanos and U. Lombardo, "Poles of inaccessibility: A calculation algorithm for the remotest places on earth," *Scottish Geographical J.*, vol. 123, no. 3, pp. 227–233, 2007.
- [61] C. E. Noon and J. C. Bean, "An efficient transformation of the generalized traveling salesman problem," *INFOR: Inf. Syst. Oper. Res.*, vol. 31, no. 1, pp. 39–44, 1993.
- [62] S. Lin and B. W. Kernighan, "An effective heuristic algorithm for the traveling-salesman problem," *Operations Res.*, vol. 21, no. 2, pp. 498–516, 1973.
- [63] M. Dorigo and M. Birattari, *Ant Colony Optimization*. Berlin, Germany: Springer, 2010.
- [64] S. Ferrari and G. Foderaro, "A potential field approach to finding minimum-exposure paths in wireless sensor networks," in *Proc. IEEE Int. Conf. Robot. Autom.*, 2010, pp. 335–341.
- [65] J. C. Isaacs, "Unsupervised domain transfer of latent dirichlet allocation derived representations from synthetic aperture sonar imagery," *Proc. SPIE*, vol. 8709, 2013, Art. no. 87090G.
- [66] P. T. Gough and D. W. Hawkins, "Imaging algorithms for a strip-map synthetic aperture sonar: Minimizing the effects of aperture errors and aperture undersampling," *IEEE J. Ocean. Eng.*, vol. 22, no. 1, pp. 27–39, Jan. 1997.
- [67] J. Weaver, J. Perkins, and D. Sternlicht, "Advanced autonomy architecture for maritime applications AVA," in *Proc. MTS/IEEE OCEANS Conf.*, Monterey, CA, USA, 2016, pp. 1–8.
- [68] M. Snyder, J. N. Weaver, and M. J. Bays, "ROS-IVP: Porting the interval programming suite into the robot operating system for maritime autonomy," in *Proc. MTS/IEEE OCEANS Conf.*, Monterey, CA, USA, 2016, pp. 1–6.
- [69] B. Nguyen, M. J. Bays, A. Shende, and D. J. Stilwell, "An approach to subsea survey for safe naval transit," in *Proc. MTS/IEEE OCEANS KONA Conf.*, 2011, pp. 1–6.
- [70] M. J. Bays, "Stochastic motion planning for applications in subsea survey and area protection," Ph.D. dissertation, Dept. Mech. Eng. Virginia Tech, Blacksburg, VA, USA, 2012.
- [71] J. R. Stack and C. M. Smith, "Combining random and data-driven coverage planning for underwater mine detection," in *Proc. IEEE Oceans Conf.*, 2003, vol. 5, pp. 2463–2468, doi: [10.1109/OCEANS.2003.178298](https://doi.org/10.1109/OCEANS.2003.178298).
- [72] T. Qin *et al.*, "Underwater archaeological investigation using ground penetrating radar: A case analysis of Shanglinhu Yue Kiln sites (China)," *J. Appl. Geophys.*, vol. 154, pp. 11–19, 2018.



**Jaejeong (Jane) Shin** (Member, IEEE) received the M.S. and Ph.D. degrees in mechanical engineering from Cornell University, Ithaca, NY, USA, in 2019 and 2021, respectively, and the B.S. degree in naval architecture and ocean engineering from Seoul National University, Seoul, South Korea, in 2017.

She has been an Assistant Professor with the Department of Mechanical and Aerospace Engineering, University of Florida, Gainesville, FL, USA, since 2021. Her research interests encompass information theoretic learning, computational geometry, motion

planning, machine learning, and optimization.



**Shi Chang** (Student Member, IEEE) received the B.S. degree in mechanical engineering from Pennsylvania State University, State College, PA, USA, in 2017. He is currently working toward the Ph.D. degree in mechanical engineering with the Laboratory for Intelligent Systems and Controls (LISC), Cornell University, Ithaca, NY, USA.

His research interests include computer vision, machine learning, information theory, and information-driven path planning of robots.

**Joshua Weaver** (Member, IEEE) received B.S. degree in electrical engineering from Florida State University, Tallahassee, FL, USA in 2007, and the M.S. and Ph.D. degrees in electrical and computer engineering from the University of Florida, Gainesville, FL, USA, in 2012 and 2014 respectively.

He currently works as a Senior Scientist for Autonomy at the Naval Surface Warfare Center in Panama City, Florida (NSWC PCD). He is the principal investigator on multiple unmanned systems projects that focus on developing autonomy architectures, behaviors, world models, and perception algorithms. His current work also includes supporting the Office of Naval Research (ONR) as well as developments in the international community.

**Jason C. Isaacs** received the Ph.D. degree in electrical engineering from the Florida State University, Gainesville, FL, USA, in 2008.

Since 2008, he has been a Research Engineer with the Science, Technology, Analysis, and Simulation Division, Naval Surface Warfare Center (NSWC PCD), Panama City, FL, USA. His research is focused on the use of machine learning, computer vision, and image processing for automatic target recognition applications. Specific areas of interest are in representational learning, knowledge transfer, and graph-based methods for shape analysis.



**Bo Fu** (Member, IEEE) received the Ph.D. degree in mechanical and aerospace engineering from the University of California, Davis, CA, USA, in 2016.

He is currently the Founder of Oiler (Oiler Equation, Inc.), Houston, TX, USA, a startup company focused on delivering the next generation innovative and intelligent gas detection solutions for the oil and gas industry. He was a Postdoctoral Associate with the Laboratory for Intelligent Systems and Controls (LISC), Cornell University, Ithaca, NY, USA, where

his work focused on applied machine learning, computer vision, and image sciences. His current research focuses on image-based algorithm development for optical gas imaging (OGI) systems.



**Silvia Ferrari** (Senior Member, IEEE) received the B.S. degree from Embry-Riddle Aeronautical University, Daytona Beach, FL, USA, in 1997, and the M.A. and Ph.D. degrees from Princeton University, Princeton, NJ, USA, in 1999 and 2002, respectively.

She is currently the John Brancaccio Professor of Mechanical and Aerospace Engineering with Cornell University, Ithaca, NY, USA. Before, she was a Professor of Engineering and Computer Science with Duke University, Durham, NC, USA, and the Founder and the Director of the NSF Integrative Graduate

Education and Research Traineeship (IGERT) and Fellowship program on Wireless Intelligent Sensor Networks (WiSeNet). She is currently the Director of the Laboratory for Intelligent Systems and Controls (LISC), Cornell University, and her principal research interests include robust adaptive control of aircraft, learning and approximate dynamic programming, and optimal control of mobile sensor networks.

Dr. Ferrari is a member of ASME, SPIE, and AIAA. She is the recipient of the ONR young investigator award (2004), the NSF CAREER award (2005), and the Presidential Early Career Award for Scientists and Engineers (PECASE) award (2006).